Photoswitchable 11 nm CsCoFe Prussian Blue Analogue Nanocrystals with High Relaxation Temperature

L. Trinh, S. Zerdane, S Mazerat, N. Dia, D. Dragoe, C. Herrero, E. Rivière, L. Catala, Marco Cammarata, Eric Collet, et al.

▶ **To cite this version:**

L. Trinh, S. Zerdane, S Mazerat, N. Dia, D. Dragoe, et al.. Photoswitchable 11 nm CsCoFe Prussian Blue Analogue Nanocrystals with High Relaxation Temperature. Inorganic Chemistry, 2020, 59 (18), pp.13153-13161. 10.1021/acs.inorgchem.0c01432 . hal-03003104

HAL Id: hal-03003104
https://hal.science/hal-03003104

Submitted on 16 Nov 2020

HAL is a multi-disciplinary open access archive for the deposit and dissemination of scientific research documents, whether they are published or not. The documents may come from teaching and research institutions in France or abroad, or from public or private research centers.

L'archive ouverte pluridisciplinaire **HAL**, est destinée au dépôt et à la diffusion de documents scientifiques de niveau recherche, publiés ou non, émanant des établissements d'enseignement et de recherche français ou étrangers, des laboratoires publics ou privés.

Photo-Switchable 11 nm CsCoFe Prussian Blue Analogue Nanocrystals with High Relaxation Temperature

*Linh Trinh, Serhane Zerdane, Sandra Mazérat, Nada Dia, Diana Dragoe, Christian Herrero, Eric Rivière, Laure Catala, Marco Cammarata, Eric Collet, Talal Mallah**

Dr. L. Trinh, S. Mazérat, N. Dia, Dr. D. Dragoe, Dr. C. Herrero, Dr. E. Rivière
Prof. L. Catala, Prof. T. Mallah
Institut de Chimie Moléculaire et des Matériaux d'Orsay
Université Paris-Saclay, CNRS
15, rue Georges Clémenceau
91405, Orsay Cedex, France
e-mail : talal.mallah@universite-paris-saclay.fr, talal.mallah@u-psud.fr

Dr. S. Zerdane, Dr. M. Cammarata, Prof. E. Collet
Univ Rennes 1, CNRS
IPR (Institut de Physique de Rennes), UMR 6251
F-35042 Rennes, France

Abstract: Photo-switchable 11 nm nanocrystals of the coordination network Cs{Co[Fe(CN)$_6$]} were obtained using a template-free method. The nanocrystals were recovered from the colloidal solutions as solid materials surrounded by cetyltrimethylammonium (CTA) cations or embedded in the organic polymer polyvinylpyrrolidone (PVP). Complementary magnetic, spectroscopic and structural techniques, including EPR Spectroscopy, reveal a majority (≈70%) of the low spin and photoactive diamagnetic $Co^{III}Fe^{II}$ pairs located in the core of the nanocrystals and a mixture of $Co^{II}Fe^{II}$ and $Co^{II}Fe^{III}$ species present mainly within the shell of the objects. While bulk compounds with similar vacancy concentration do not exhibit noticeable photoinduced charge transfer, the obersved photoactivity of the nanocrystals is ascribed to their nanometric size. The relaxation temperature of the photo-induced state shifts upwards by ≈ 55 K when PVP is replaced by CTA. This is ascribed to the larger rigidity of the dense CsCoFe_CTA material whose metastable state is lower than for CsCoFe_PVP leading to a larger relaxation energy barrier and, therefore, to higher relaxation temperature.

INTRODUCTION

Prussian blue analogues (PBA) were and still are at the forefront in the area of switchable molecular materials because of their versatile physical and chemical properties that can be tuned and monitored by external stimuli such as temperature, light, electric and magnetic fields,[1-6] opening the route for applications in a wide range of domains. Recently, these systems emerged as efficient cathode materials for sodium containing batteries controlled by an electric potential.[7, 8] But, the most attractive properties are optical and the most efficient stimulus turned out to be light irradiation that tunes the electronic structure of the materials, allowing the emergence of new functionalities and therefore applications in catalysis,[9, 10] medicine[11-13] and information[14], particularly when the materials are shaped at the nanoscale.[15] Therefore, designing nanocrystals of light responsive PBA possessing well-defined shape, size and composition is timely to get deep insight into the relation between electronic structure and physical behavior and their impact on the emergence of novel functionalities.

Accepted Manuscript

The CoFe based analogue is one of the most studied since its discovery by Hashimoto *et al.* in 1996,[2] due to its versatile and tunable chemical composition and its large response to light.[16-19] Red (and green) light induces an electron transfer from Fe^{II} to Co^{III} allowing the transformation of the diamagnetic low spin $Co^{III}Fe^{II}$ (low spin, *LS*, $S = 0$ for $t_{2g}^6e_g^0$ Co^{III} and Fe^{II} configurations) state to the ferrimagnetic metastable $Co^{II}Fe^{III}$ (high spin, *HS*, $S = 3/2$ for Co^{II}, $t_{2g}^4e_g^2$ and low spin $S = ½$ for Fe^{III}, $t_{2g}^5e_g^0$) one. This electron transfer is accompanied by a color change and an expansion of the lattice due to the *LS* to *HS* conversion, the (*HS*)Co^{II}–N bond lengths being larger than the (*LS*)Co^{III}–N ones. Even though the effect is efficient at low temperature where the metastable state has a long lifetime, irradiating a solution containing nanoparticles of this material allowed the observation of water oxidation and oxygen evolution,[10, 20] demonstrating the dual impact of size and electronic structure on the physical behavior of the objects even at room temperature.

The study of very small and well-crystallized CoFe objects in the 10 nm size range is rare, it mainly focused on nanoparticles grown within organic or inorganic matrices.[21-25] To the best of our knowledge, perfectly dispersible template-free CoFe nanocrystals in the 10 nm range have not been reported to date. The added-value of such nano-objects is the possibilities offered by their manipulation in solution like molecules, their use to prepare single layers on different substrates and ultimately their integration in devices. Moreover, they may present a modified behavior than the bulk as a consequence of their nanometer size.

Here, we report, the preparation and the full characterization of template-free 11 nm CoFe based nanocrystals (noted CsCoFe). We demonstrate, using complementary techniques (X-ray diffraction, electronic spectroscopies and magnetic measurements), a synergetic effect between the *nanometric size* of the objects and their *environment* that has a major impact on their elastic and electronic properties. By engineering a chemical embedding, we succeeded in shifting upward by 55 K the relaxation temperature of the photo-induced state when replacing the soft polyvinylpirridine (PVP) polymer by cetyltrimethylammonium (CTA) around the nanocrystals.

RESULTS

Prussian blue analogues form three dimensional networks made of octahedral hexacyanometallate species surrounded by six metal ions and vice-versa leading to a face centered cubic (fcc) structure with a cell parameter close to 10 Å corresponding to the M-CN-M'-CN-M distance. The tetrahedral sites have the right volume to accommodate Cs^+, even though other alkali ions (Rb^+) can also be inserted. For most of the networks with a localized valence, the oxidation state of M and M' are III and II respectively. However, for some cases,[26, 27] and particularly when M = Fe and M' = Co, it is possible to access two mixed valence states, namely $Co^{III}Fe^{II}$ and $Co^{II}Fe^{III}$ that have close energies and different entropies, opening the possibility of switching from one to another using external perturbations such as temperature and light.

Preparation and characterization

Template-free Prussian Blue analogue nanocrystals were prepared as negatively charged objects when solutions of $K_3[Fe^{III}(CN)_6]$ and $[Co^{II}(H_2O)_6]Cl_2$ are rapidly mixed in the presence of an excess of CsCl in water (see SI for details of the preparation).[28, 29] Dynamic Light Scattering (DLS) (Figure S1) of the as-prepared colloidal solution shows objects with a hydrodynamic diameter centered at around 12 nm. Transmission Electronic Microscopy (TEM) imaging (Figure 1) reveals the presence of nano-objects with a size of 11.0 ± 1.5 nm confirming the DLS measurement.

Accepted Manuscript

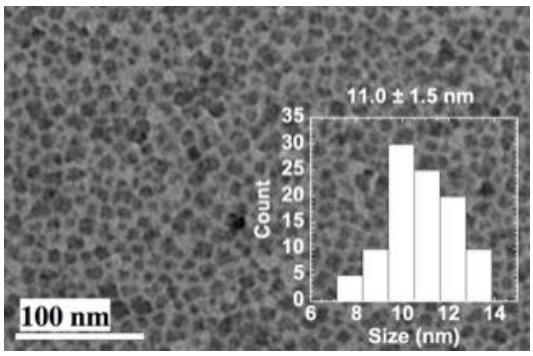

Figure 1. Transmission Electron Microscopy image of the as-prepared CsCoFe nanocrystals and size distribution (inset).

The nanocrystals were recovered from solution as solid materials by cetyltrimethylammonium Bromide (CTABr) or by the organic polymer polyvinylpyrrolidone (PVP) noted CsCoFe_CTA (**1**) and CsCoFe_PVP (**2**), respectively (see SI for details of the preparation). The main difference between **1** and **2** is the nature of the surroundings and the concentration of nanoparticles in the solid material that is much lower in the latter than in the former as we already reported on other systems.[30] We, also, prepared nanocrystals of reference compounds namely $Cs_2Co^{II}Fe^{II}$ (**3**) containing paramagnetic Co^{II}, and the alkali free $Co^{II}Fe^{III}_{0.66}$ NPs (**4**) containing magnetic $Co^{II}Fe^{III}$ pairs. DLS measurements confirmed the presence of nanocrystals with sizes of 50 and 200 nm for $Cs_2Co^{II}Fe^{II}$ (**3**) and $CoFe_{0.66}$ (**4**) respectively (Figure S1).

Energy Dispersive X-ray Spectroscopy (EDS) (Table S1) for CsCoFe_CTA (**1**), $Cs_2Co^{II}Fe^{II}$ (**3**) and $CoFe_{0.66}$ (**4**) and elemental analysis (see SI) allow us to determine the following chemical formula: $(CTA)_{0.4}[Cs_{0.7}Co\{Fe(CN)_6\}_{0.9}]\bullet H_2O_{0.6}$, $[Cs_{1.8}Co\{Fe(CN)_6\}_{0.95}]\bullet 0.5H_2O$ and $[Co\{Fe(CN)_6\}_{0.66}]\bullet 3H_2O$ for **1**, **3** and **4**, respectively. For **1**, the amount of water molecules was determined by a Thermo Gravimetric Analysis study (Figure S2). For CsCoFe_PVP (**2**), EDS gives a Co/Fe ratio close to 1, the amount of PVP being very large no further analysis was made on **2**. As the particles from the same batch were recovered both by CTABr and PVP, their composition was therefore reasonably assumed to be the same.

The infra-red spectrum of Cs_2CoFe (**3**) in the 2300 – 2000 cm^{-1} region (Figure S3), corresponding to the asymmetric elongation of the cyanide group, evidences a vibration band (2092 cm^{-1}) characteristic of the $Co^{II}Fe^{II}$ species.[31] The shoulder at 2060 cm^{-1} is attributed to non-bridging cyanides that belong the particles' surface. For $CoFe_{0.66}$ (**4**) (Figure S4), the main band at 2160 cm^{-1} is characteristic of the $Co^{II}Fe^{III}$ species, and two very weak bands at 2119 and 2092 cm^{-1} correspond to $Co^{III}Fe^{II}$ and $Co^{II}Fe^{II}$ pairs respectively.[31] The intrinsic intensities of the bands corresponding to these last two species are around 10 times and 4 times larger, respectively, than that of $Co^{II}Fe^{III}$.[31] The contribution of the $Co^{III}Fe^{II}$ and $Co^{II}Fe^{II}$ species to **4** is, thus, negligible. The infra-red spectrum of CsCoFe_CTA (**1**) (Figure S5) shows an intense band at 2114 cm^{-1} closer in energy to 2119 cm^{-1} than to 2092 cm^{-1} indicating the presence of a larger amount of $Co^{III}Fe^{II}$ than $Co^{II}Fe^{II}$ species in **1**. The shoulder at 2060 cm^{-1} is due to terminal non-bridging cyanides linked to Fe^{II}. Another weak band is present at 2176 cm^{-1}, a frequency slightly larger than 2160 cm^{-1}, that was tentatively assigned to non-linear Co^{II}–NC–Fe^{III} species belonging to the particles' surface. The much weaker intensity of the cyanide vibration band when cyanide is linked to Fe^{III} than when linked to Fe^{II} indicates that the amount of the $Co^{II}Fe^{III}$ species is not negligible within the nanocrystals of **1**.[31] Unfortunately, it is difficult to get a quantitative estimation of these $Co^{II}Fe^{III}$ pairs from the infra-red data, but magnetic and X-ray powder diffraction data provide quantitative information (see below). In summary, infra-red spectroscopy indicates that the diamagnetic $Co^{III}Fe^{II}$ pairs are the major species in CsCoFe_CTA (**1**) and that $Co^{II}Fe^{II}$ and $Co^{II}Fe^{III}$ pairs are present as minor species, but in non-negligible amount.

The analysis of the X-ray powder diffraction diagrams of Cs_2CoFe (**3**) and $CoFe_{0.66}$ (**4**) gives cell parameters values of 10.33 and 10.28 Å, respectively (Figure S6). For CsCoFe_CTA (**1**) (Figure S7),

Accepted Manuscript

the cell parameter was found equal 10.03±0.05 Å closer to the value corresponding to a pure $CsCo^{III}Fe^{II}$ network (9.95 Å) than to Co^{II} containing networks indicating the presence of a majority of the $Co^{III}Fe^{II}$ species. This is consistent with the infra-red data. Because the Bragg peaks are rather symmetrical, one can assume that the overall cell parameter is averaged over the objects. It is, then, possible to estimate a 28% contribution of the Co^{II} containing species ($Co^{II}Fe^{III}$ and $Co^{II}Fe^{II}$), on one hand, and 72% of the $Co^{III}Fe^{II}$ network, on the other hand, which correspond to a Co^{III}/Co^{II} ratio of 2.6. It is worth noting that a cell parameter value of 10.03±0.05 was found for a bulk material containing a 70/30 : Co^{III}/Co^{II} ratio and a Cs/Co ratio of 0.97 validating our results.[18] A correlation length of 10.5 nm was determined using Scherrer equation for CsCoFe_CTA (**1**), which is consistent with the sizes determined from DLS and TEM analysis.

In order to assess the composition of the nanocrystals' surface, we performed X-ray Photoelectron Spectroscopy (XPS) analysis of the objects assembled as a thin film on a Highly Oriented Pyrolytic Graphite (HOPG) substrate (see SI). Atomic Force Microscopy (AFM) imaging shows a laterally dense layer of nanoparticles (Figure S8) with an average height close to 12 nm including regions with heights around 23 nm, indicating the presence of a single layer of particles and some bilayers.

XPS allows investigating both the atomic ratio of the different elements, and the oxidation state for a given element. The XPS spectra show the presence of both Co^{III} and Co^{II} species (Figure 2) together with all the other elements N, Fe and Cs (Figure S9). The quantitative analysis of the spectra leads to Co/Fe and N/Fe ratio close to 1 and 7 as expected. The Co^{III}/Co^{II} ratio was estimated by fitting two main symmetrical lineshapes for each Co^{II} and Co^{III} state and two large peaks approximating the shake-up satellites (not shown in Figure 2) and was found equal to 2.0. We observed a slight evolution of the Co spectra with time due to reduction of some Co^{III} to Co^{II} (Figure S10), which allowed to extrapolate a Co^{III}/Co^{II} ratio at t = 0 of 2.16, still well below 2.6 found from XRPD data. If the metal ions were statistically distributed within the nanocrystals, the Co^{III}/Co^{II} ratio obtained from XPS should be the same as found from the XRPD data (2.6 instead of 2.16). The explanation to this discrepancy is the presence of a larger concentration of Co^{II} ions on the surface of the nanocrystals than in the bulk giving rise to a relatively more intense XPS signal for Co^{II} and, therefore, to an apparent smaller Co^{III}/Co^{II} ratio. In order to simulate the intensity of the XPS signal as a function of the film depth (d), we first determined the mean free path of electrons within the film of nanocrystals as a function d that was found equal to 1.7 nm (Figure S11).[32, 33] We then determined the Co^{III}/Co^{II} ratio for different distributions of Co^{II} within a nanocrystal of 11 nm edge size, considering both the mean free path of the electrons and the contribution of the different nanocrystal layers (see SI for the details of calculations and the definition of "layer"). A good correlation between the Co^{III}/Co^{II} ratios extracted from XRPD and XPS is obtained for a model where the Co^{II} ions are present only within a shell of 2 nm thickness of the nanocrystal and absent in its core (see SI). Bleuzen *et al.* have recently shown, using X-ray Absorption Spectroscopy, that the surface of CoFe nanoparticles (5.5 nm size) embedded in silica is mainly made of $Co^{II}Fe^{III}$ pairs where the metal ions have a distorted environment.[34] Our results are consistent with these findings.

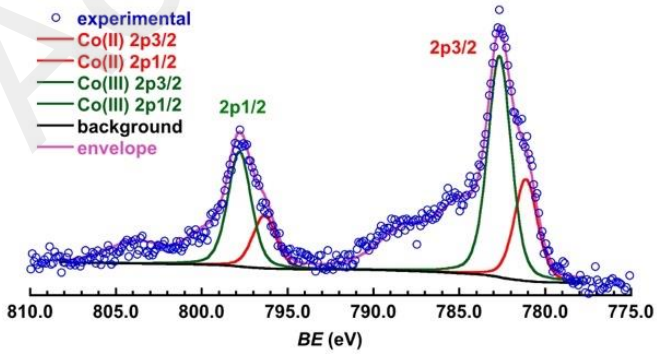

Figure 2. XPS spectrum at the 2p edge of Co for the as-prepared objects assembled on HOPG.

Accepted Manuscript

Assessing the nature of the metastable state by X-ray diffraction and optical studies

The X-ray diffraction studies were performed on CsCoFe_PVP (**2**) where the particles are embedded in PVP using a film with a thickness of a few microns in order to maximize the light induced transformation thanks to the transparency of the film. XRD patterns were collected using 4-circle diffractometer at IPR with monochromatic radiation (λ = 0.71073 Å). The diffraction patterns were measured before, during and after irradiation and are characteristic of the fcc structure (Figure 3a). The large background in the scattered signal is due to PVP. The cell parameter (*a*) before irradiation was found to be equal to 10.068 Å. The PVP film containing the nanoparticles were then irradiated with a green laser (532 nm, with a beam spot of ≈ 5 mm^2). Upon irradiation (28 mW, *T* = 10 K) the cell parameter *a* increases, almost exponentially with a time constant of 4.7 min^{-1}, saturates around 10.145 Å and remains almost constant once laser excitation is switched off (Figure 3b). This lattice expansion is characterized by the shift of the Bragg peaks towards lower scattering vector Q (inset of Figure 3a). The Bragg peaks keep similar width before, under or after laser excitation, which indicates both a *global conversion* of the particles within the film and a *homogeneous excitation* within the particles. It also shows that *all the particles* within the films were photoexcited as, after photoexcitation, there is no more diffraction signal at the original position of the Bragg peaks before laser excitation. This photoinduced state is long-lived. Under stronger laser excitation (100 mW) a (laser) heating effect is observed, characterized by an additional shift of the peaks toward lower Q as the cell parameter reaches 10.16 Å, but once laser excitation is switched off, the cell parameter (*a*) recovers rapidly its original value before heating 10.145 Å (dashed line, Figure 3b). This experiment confirms that the maximal conversion was already reached after ≈20 min of laser excitation at 28 mW. The photoinduced electron transfer phenomenon being concomitant with the spin crossover on the Co sites induces an elongation of the Co-N bonds of ≈0.18 Å and therefore a lattice expansion of the unit cell parameter of ≈0.36 Å. The experimentally observed lattice expansion of 0.077 Å, from *a* = 10.068 Å to 10.145 Å, corresponds therefore to a ≈21% conversion of the $Co^{III}Fe^{II}$ species (from ≈67 to ≈45%) leading to a relative transformation of about 30% from of the diamagnetic $Co^{III}Fe^{II}$ species to the paramagnetic $Co^{II}Fe^{III}$ one. We observed similar lattice expansion under laser irradiation at 660 nm at 80 K, for both CsCoFe_CTA (**1**) and CsCoFe_PVP (**2**) (Figure S12). Once laser excitation is switched off, the lattice parameter in CsCoFe_PVP (**2**) relaxes faster than in CsCoFe_CTA (**1**), which seems to indicate a stronger stabilization of the photoinduced state in CsCoFe_CTA (**1**), as discussed hereafter with magnetic measurements.

We, also, measured the optical spectra changes on the same thin film of CsCoFe_PVP (**2**) used for the X-ray diffraction. The optical density (OD) measurements were performed at *T* = 15 K before and after laser excitation at λ = 660 nm (Figure 4). The differential OD (black trace) corresponding to the difference between the spectra after (red trace) and before (blue trace) excitation reveals the appearance of two bands around 610 and 430 nm that can be attributed to the photoinduced state $Co^{II}Fe^{III}$. The negative absorption at 520 nm in the differential spectrum is, therefore, a signature of an absorption within the ground diamagnetic $Co^{III}Fe^{II}$ state. This experiment demonstrates that the large band of CsCoFe_PVP (**2**) (blue trace in Figure 4) observed in the 650-500 nm region is composed of two bands, one at 520 nm due to the $Co^{III}Fe^{II}$ species (majority species) and the other at 610 nm due to $Co^{II}Fe^{III}$ (minority species) both present in the nanocrystals before irradiation. This is consistent with the IR and XRPD data that the two mixed valence species $Co^{II}Fe^{III}$ and $Co^{III}Fe^{II}$ are both present in the nanocrystals. The $Co^{II}Fe^{II}$ species do not exhibit any detectable absorption in this region, but Electron Paramagnetic Resonance (EPR) Spectroscopy allows detecting and quantifying these species, as demonstrated hereafter.

Accepted Manuscript

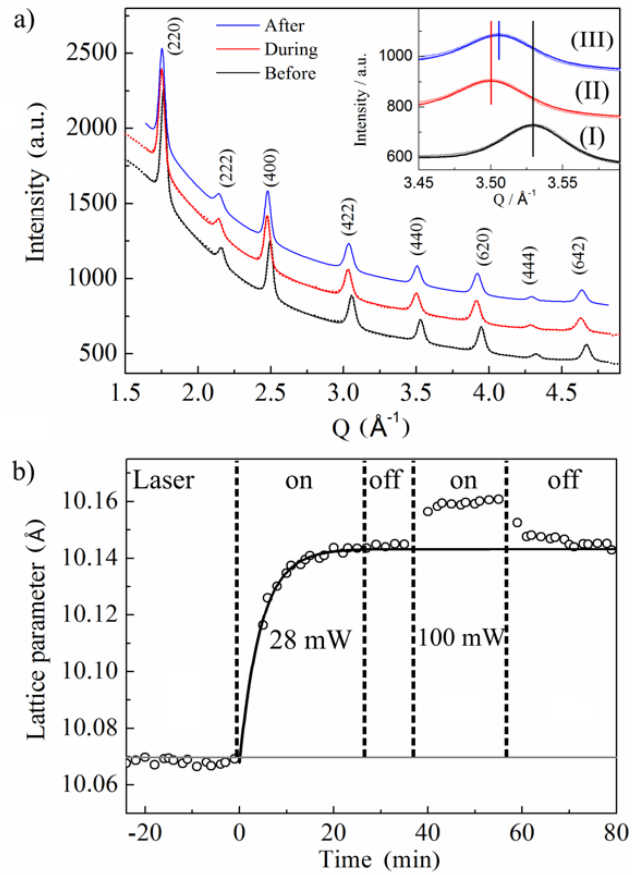

Figure 3. (a) X-ray powder diffraction pattern of CsCoFe_PVP (**2**), characteristic of the fcc lattice, before, during (100 mW) and after irradiation at 532 nm. The inset shows the shift of the Bragg peak due to photoswitching or laser heating, (b) evolution of the lattice parameter with laser excitation. The continuous line is an exponential fit of the lattice expansion.

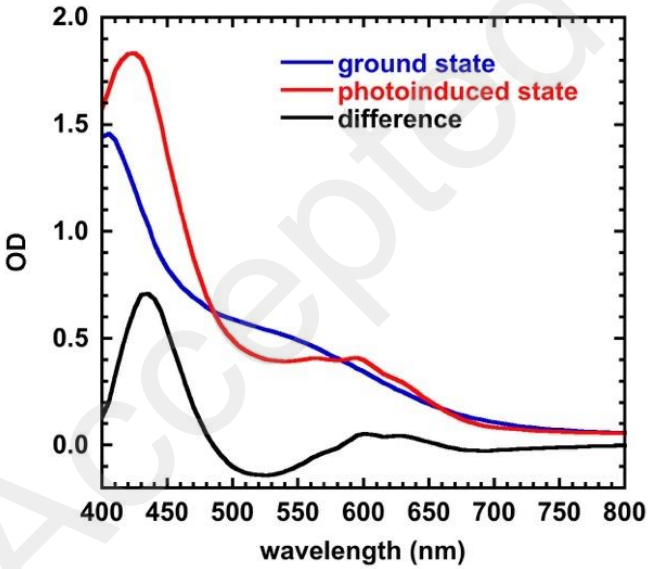

Figure 4. Optical spectra of CsCoFe_PVP (**2**) in the ground state (blue trace), in the photoinduced state (red trace) after irradiation at 660 nm and differential spectra (black trace).

Detection of the paramagnetic $Co^{II}Fe^{II}$ species by EPR

All EPR experiments were carried out on freshly prepared colloidal aqueous solutions containing the nanocrystals. We first performed the EPR study on the reference compound $Cs_2Co^{II}Fe^{II}$ (**3**) that shows a resonance at g = 4.1 (T = 10 K) typical of high spin Co^{II} (S = 3/2) in a distorted octahedral environment (Figure S13).[35] The nanocrystals of $Co^{II}Fe^{III}_{0.66}$ (**4**) did not show any resonance down to

Accepted Manuscript

T = 10 K (Figure S13), indicating that when Co^{II} ions are directly linked to the paramagnetic $Fe^{III}(CN)_6$ (*S* = ½) species, they are EPR silent. Exchange coupling interactions between the two paramagnetic ions (Co^{II} and Fe^{III}) through the cyanide bridge may broaden the signal (see magnetic measurements below). These two studies lead to the conclusion that high spin Co^{II} ions (*S* = 3/2) can be detected by EPR *only when they are magnetically isolated* within the network, i.e., when they are surrounded by water molecules and/or diamagnetic low spin $Fe^{II}(CN)_6$.

The EPR spectrum of the CsCoFe nanocrystals dispersed in water (without CTA or PVP, Figure 5) has a single resonance at *g* = 4.1 with the same shape as for the reference sample $Cs_2Co^{II}Fe^{II}$ (**3**), confirming that within the nanocrystals (i) there are isolated Co^{II} paramagnetic species and (ii) their coordination sphere is almost identical to that of the reference sample $Cs_2Co^{II}Fe^{II}$ (**3**). A quantification of the EPR signal based on the intensity of the resonance of $Cs_2Co^{II}Fe^{II}$ (**3**), whose concentration in Co^{II} is known, shows that the CsCoFe nanocrystals contain 10% of isolated paramagnetic Co^{II} ions.

The dispersion of the CsCoFe nanocrystals was irradiated at 635 nm (*T* = 10 K) and the spectra registered after 5, 10 minutes and longer times and after relaxation at 200 K. The intensity of the EPR band decreases very rapidly after 5 minutes and then slightly further after 10 minutes where saturation was observed (Figure 5). The intensity of the spectrum decreases by 75% demonstrating that the isolated Co^{II} ions (surrounded by diamagnetic $Fe^{II}(CN)_6$ species in the dark state) become silent after irradiation. This is due to the photo-transformation of diamagnetic $Fe^{II}(CN)_6$ entities linked to the isolated Co_i^{II} (the index *i* indicates magnetically isolated Co^{II} ions) to paramagnetic ones ($Fe^{III}(CN)_6$) leading to the formation of Fe^{III}–CN–Co_i^{II} pairs that become EPR silent. From the structural point of view, this is consistent with a close contact (one coordination bond) between the $Co^{III}Fe^{II}$ and the $Co_i^{II}Fe^{II}$ pairs within the nanoparticles as tentatively depicted in Scheme 1.

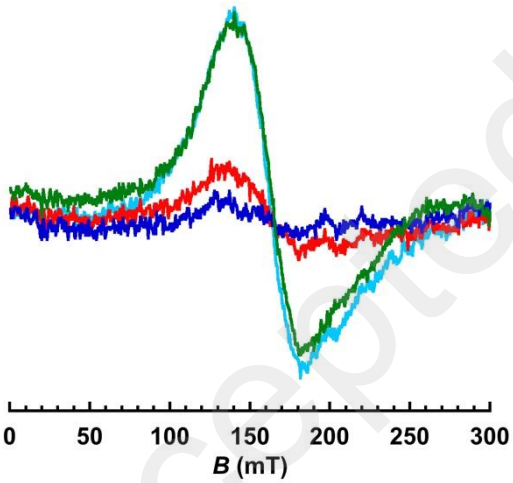

Figure 5. EPR spectra of the as-prepared nanocrystals (before recovering by CTA) at *T* = 10 K before irradiation (light blue), after irradiation for 5 minutes (red) and for 10 minutes (blue) and then after relaxation by heating the solution to 200 K and then cooling to 10 K (green), (experimental conditions (microwave frequency = 9.63 GHz, modulation amplitude = 8 G, microwave power = 1.00 mW, modulation frequency 100 KHz, gain = 34 dB).

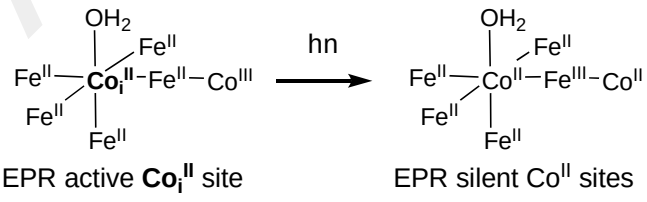

Scheme 1. Schematic illustration of the position of an EPR active Co_i^{II} site coordinated to a diamagnetic Fe^{II}–CN–Co^{III} pair that becomes silent after electron transfer upon irradiation

Accepted Manuscript

Magnetic and photomagnetic behavior

We investigated the magnetic properties of CsCoFe_CTA (**1**) and CsCoFe_PVP (**2**) with the objective of assessing the effect of chemical environment on their photomagnetic behavior. We measured the properties of the two reference compounds $Cs_2Co^{II}Fe^{II}$ (**3**) and $Co^{II}Fe^{III}_{0.66}$ (**4**) that are detailed in the Supporting Information (Figure S14 and S15).

For CsCoFe_CTA (**1**), the χT = f(T) plot (Figure 6a and Figure S16) has a value of 0.83 emu K / mol at T = 250 K. This value is consistent with the spin only value expected (0.98 emu K / mol) for the amount of paramagnetic Co(II) ions (see SI for additional comments). A maximum at T = 7 K is observed consistent with the presence of $Co^{II}Fe^{III}$ pairs within the nanoparticles because if only isolated paramagnetic Co_i^{II} species were present χT would decrease upon cooling (see Figures S14 and S15 for comparison). The temperature of the maximum of χT (7 K) is well below that of $Co^{II}Fe^{III}_{0.66}$ (**4**) (12 K) indicating a much shorter magnetic correlation length for CsCoFe_CTA (**1**) than for $Co^{II}Fe^{III}_{0.66}$ (**4**) leading to the conclusion that the $Co^{II}Fe^{III}$ pairs are relatively isolated in CsCoFe_CTA (**1**).

The sample was irradiated at T = 10 K (635 nm, power 20 mW/cm^2) for 3 hours until saturation was observed. Then, the light was switched off, the temperature decreased to 2 K and the magnetization measured while heating which allows us to plot the χT = f(T) curve (Figure 6a, Figure S16). χT has the behavior usually observed for photoswitchable CoFe material, a maximum is observed at T = 14 K due to a much longer magnetic correlation length than before irradiation. Upon heating up, χT decreases from 6.6 emu K / mol, reaches a value of 2.2 emu K / mol at 55 K where a quasi-plateau is observed until T = 65 K. Then χT decreases and reaches its value before irradiation at around T = 150 K (Figure 6a, inset), which is defined as the relaxation temperature T_{relax}*(CTA)* for CsCoFe_CTA (**1**). Above this temperature, the two curves before and after irradiation are superimposable within experimental error. The sample was then cooled down from room temperature to T = 2 K, the curve after relaxation is almost identical to the one before irradiation showing the reversibility of the process. The temperature of the maximum of χT shifts from 7 to 14 K due interparticle dipolar ferromagnetic interactions as we have already shown on other PBA nanocrystals.[30] The detailed study of this collective behavior is out of scope of this paper and will be the subject of another report.

The magnetization vs. the applied magnetic field (B) was measured before and after irradiation and after relaxation (Figure 6b). An increase of the magnetization of 0.7 Bohr Magneton is observed at B = 6 T due to the transformation of $Co^{III}Fe^{II}$ pairs to $Co^{II}Fe^{III}$. Assuming 10% concentration of $Co^{II}Fe^{II}$ pairs as found from EPR, it is possible to compute a concentration of 22% for $Co^{II}Fe^{III}$ pairs before irradiation considering the magnetization values of CsCoFe_CTA (**1**), $Cs_2Co^{II}Fe^{II}$ (**3**) and $Co^{II}Fe^{III}_{0.66}$ (**4**) at 6 T, which is consistent with the values found from the XRPD data (see above). After irradiation, the concentration of the $Co^{II}Fe^{III}$ pairs increases to 54% showing a transformation of 32% $Co^{III}Fe^{II}$ pairs to $Co^{II}Fe^{III}$, which corresponds to a relative transformation of 0.32/0.68 = 47%. Another way to estimate the relative photo-conversion without any assumption is to compute the $(M_a\text{-}M_b)/M_a$ ratio where M_a and M_b are the experimental magnetization values at B = 6 T after and before irradiation equal to (1.38-0.68)/1.38 = 50% consistent with the previous value.

Accepted Manuscript

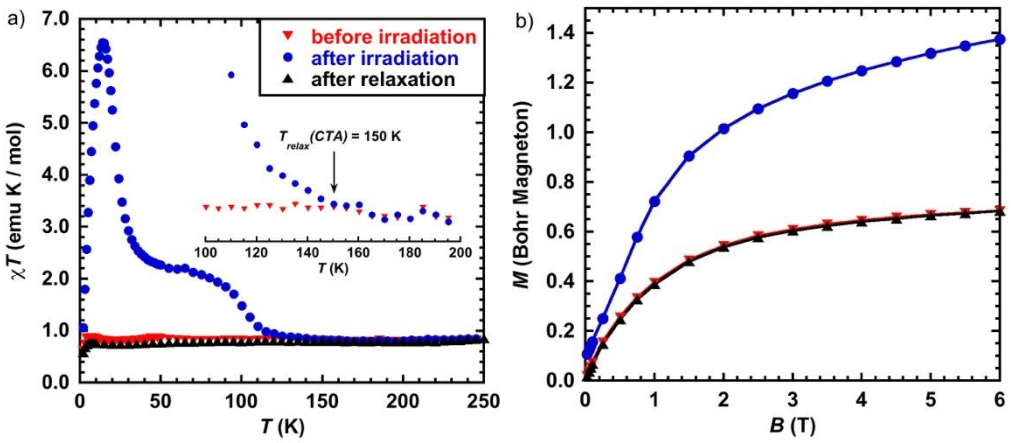

Figure 6. Magnetic data for CsCoFe_CTA (**1**), (a) χT = f(T), the inset shows the relaxation temperature after irradiation and (b) M = f(B) at T = 2 K before (▼) and after (●) irradiation at T = 10 K and after relaxation (▲) at T = 300 K.

For *CsCoFe_PVP* (**2**), the χT = f(T) (Figure 7a) curves are similar to those of CsCoFe_CTA (**1**) The maximum, after irradiation, at T = 9 instead of 14 K for CsCoFe_CTA (**1**) suggests a shorter magnetic correlation length ascribed to weaker interparticle dipolar ferromagnetic interactions,[30] confirming that the nanocrystals are more diluted in **2** than in **1.** The relaxation temperature (T_{relax}*(PVP))* was determined to be equal to 95 K (Figure 7a, inset). The magnetization data (Figure 7b) show, upon irradiation, an increase from 0.4 to 0.51 emu / g (at 6 T) corresponding to a relative conversion of 21%, a value consistent with that found from the XRPD data.

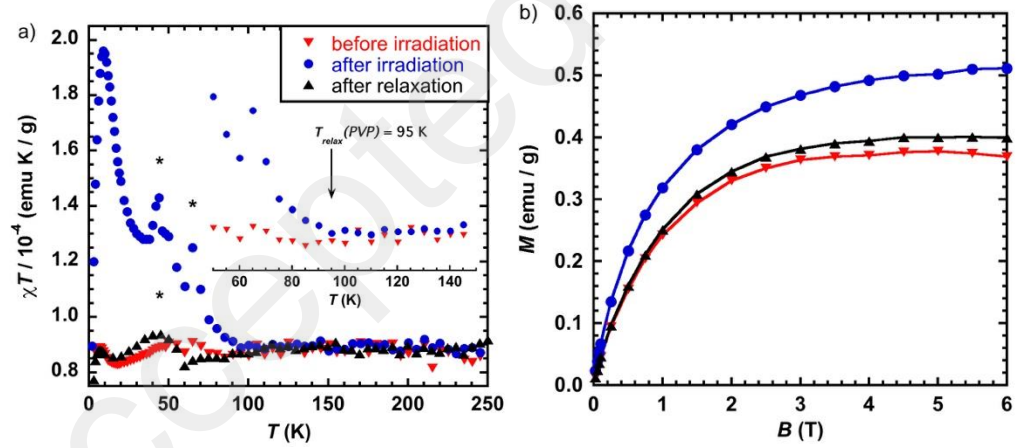

Figure 7. Magnetic data for CsCoFe_PVP (**2**), (a) χT = f(T), the inset shows the relaxation temperature after irradiation and (b) M = f(B) at T = 2 K before (▼) and after (●) irradiation and after relaxation (▲). *in the 40 – 70 K region the bumps are due to the presence of some oxygen gas trapped in the organic polymer that we observe in some experiments.

Accepted Manuscript

DISCUSSION

Role of the alkali ion and vacancies

An important feature of the nanocrystals is the large Cs^+ concentration and, consequently, the small amount of vacancies when compared to bulk systems that are photoactive (0.7 here in comparison to 0.17 and 0.3 for Cs/Co ratio and 10% here in comparison to 28% and 20% for $Fe(CN)_6$ vacancies).[17, 18] Actually, bulk systems with Cs/Co ratios equal to 0.57 and 0.97 and vacancies of 15% and 3%, similar to the present nanocrystals, are low spin over the whole temperature range and are not photoactive. While the 11 nm nanocrystals that possess a very small amount of vacancies (10%) and remain low spin up to room temperature are still photoactive.

The role of Cs^+ as templating agent was reported to be a determining factor on the nucleation and growth steps of charged PBA nanoparticles,[15] as well as for the formation of molecular cyanide-bridged cubes.[36, 37] During the formation of the nanocrystals, a large number of seeds are produced with few vacancies in hexacyanoferrate(II) that may be nearly perfect primary cubes with a central Cs^+ and linear Co-CN-Fe bonds.[38] As supported by the combined results of XPS, PXRD and EPR studies, the nanocrystals would thus comprise a well-crystallized $Co^{III}Fe^{II}$ core close to 7 nm that may be obtained from these seeds either by coalescence through coordination bonds or normal growth step around them. On these well-ordered cores, one may envisage a more distorted Co-CN-Fe environment for the terminal layers (with or without Cs) (Scheme 2). The non-linearity of the terminal Co-CN-Fe pairs and slightly different position of the Cs^+ cation in the tetrahedral sites may account for the stabilization of $Co^{II}Fe^{III}$ and $Co^{II}Fe^{II}$ at the periphery, as proposed by Bleuzen *et al.* on a $Cs_{0.18}CoFe$ bulk compound.[38]

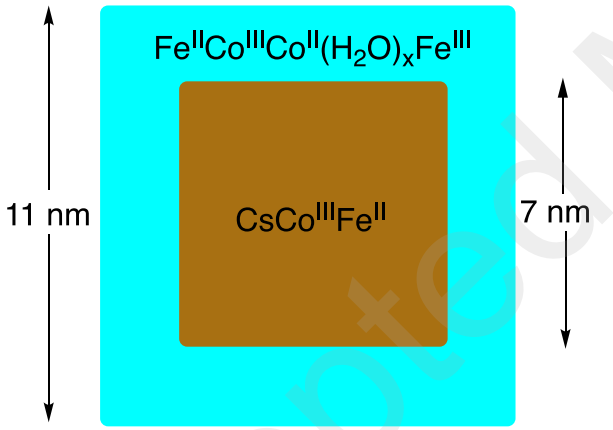

Scheme 2. Schematic view of the structure of the nanocrystals

The absence of photoactive effect in systems with a small amount of vacancies was attributed to the difficulty of the network to accommodate the large structural change and lattice expansion concomitant to the spin crossover on the Co sites accompanying the electron transfer. During the photo-induced electron transfer from the *LS* ($Co^{III}Fe^{II}$) to the *HS* state ($Co^{II}Fe^{III}$), the cell parameter increases by 4 %, which corresponds to a volume increase of 12%. Therefore, for large particles (or bulk) with almost no vacancies, the network is not flexible enough to accompany the structural change. While for small nanocrystals, despite the quasi absence of vacancies, the energy necessary to accommodate their structure is much lower than for larger objects explaining the observation of a photoresponse for nanometric objects and its absence for bulk systems.

Accepted Manuscript

Effect of environment on the magnetic and photomagnetic behavior

A striking difference between the properties of nanocrystals surrounded by CTA^+ (**1**) and those embedded in PVP (**2**) ~~concerns~~ is the relaxation temperature of the photoinduced state, which is shifted by 55 K towards high temperature for **1** in comparison to **2** ($T_{relax}(CTA)$ ≈150 K and $T_{relax}(PVP)$ ≈ 95 K, insets of Figure 6a and Figure 7b). As attested by the magnetic data, the nanocrystals are identical in the two samples because they are in the same state before irradiation, one can, thus, reasonably assume that the larger stabilization of the *LS* state in CsCoFe_PVP (**2**) is due to the nature of the matrix embedding them and more precisely to its elastic properties.[39-42] This observation agrees with the faster relaxation of the lattice parameter after irradiation at 80 K observed by X-ray diffraction (Figure S12). Indeed, in the photoinduced state, the volume of the particles, and therefore of the film, increases. The relatively soft PVP polymer can easily accommodate the elastic energy due to the volume change and the global expansion of the PVP film is weaker than for the CTA^+ film, where more densely packed nanoparticles will result in a larger volume expansion of the film. This larger expansion of the film stabilizes the larger-volume photoinduced state. The alkane chains, assumed to be interdigitated, behave as a more rigid environment able to couple the nanoparticles elastically and therefore shifts the relaxation temperature to higher values.

The difference in the relaxation temperatures can tentatively be schematized by the potential energy curves,[43] (Scheme 3) where the energy barrier for relaxation is lower in the case of the nanocrystals embedded in PVP (**2**) than when surrounded by CTA^+ (**1**), which is at the origin of the lower T_{relax} for the former than for the latter. Consequently, the energy difference between the metastable and the ground states is larger for CsCoFe_PVP (**2**) than for CsCoFe_CTA (**1**).

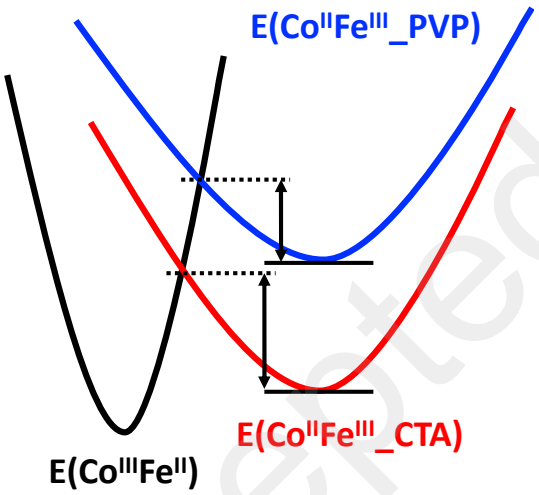

Scheme 3. Schematic effect of the polymer shifting the potential of the high-volume state due to elastic interaction.

Accepted Manuscript

CONCLUSIONS

Nanocrystals of the photomagnetic CsCoFe Prussian blue analogues with 11 nm size were prepared by a template-free coprecipitation method in water leading to well-individualized charged nanoparticles. The nanoobjects were fully characterized in solution and in the solid state when surrounded by the cetyltrimethylammonium (CTA) cation and when embedded by the organic polymer polyvinylpyrrolidone (PVP). Complementary characterization techniques reveal that the nanoobjects contain a majority of the diamagnetic $Co^{III}Fe^{II}$ network, but also the $Co^{II}Fe^{III}$ and $Co^{II}Fe^{II}$ pairs which contribute to about 30 %. The presence of the $Co^{II}Fe^{II}$ pairs is suggested by infra-red spectroscopy and evidenced quantitatively, for the first time, by EPR. Using XPS, we show that they belong mainly to the outer shell of the particles allowing us to propose a structural model for the nanocrystals.

The observation of a photoresponse despite the large Cs^+ concentration and the quasi absence of $Fe(CN)_6$ vacancies is attributed to the lower energy needed by the nanometric objects than by the larger ones to accommodate the lattice expansion upon irradiation. Consequently, the environment plays a key role where a synergetic effect due to the small size of the nanocrystals and the nature of the matrix (its compressibility and interaction with the particle's surface) leads to a larger relaxation temperature (by 55 K) for CsCoFe_CTA (**1**) than for CsCoFe_PVP (**2**).

Beyond the unique photomagnetic behavior of the nanocrystals, their stability in water as charged objects in the absence of any surfactant allows their easy manipulation to (i) investigate their magnetic properties in solution as we carried out by EPR, (ii) assemble them on a substrate of interest as we have shown here on HOPG, (iii) embed them in PVP and produce thin transparent films of good optical quality to perform photomagnetic studies and (iv) produce solid state materials where the objects sustain different environments that tune their photomagnetic behavior. Work is underway to organize them as arrays on functionalized substrates,[44, 45] and more importantly to trap them between electrodes to investigate the effect of light on their conducting behavior.

ASSOCIATED CONTENT

Supporting Information

The Supporting Information is available free of charge at
https://pubs.acs.org/doi/
Preparation of the nanocrystals, Dynamic light scattering, Thermogravimetric analysis, infra-red, XRPD under light, AFM imaging, XPS (PDF)

Author Contributions

LT, SM and ND prepared the nanocrystals performed preliminary characterization by TEM, DLS and X-ray diffraction. SM prepared the thin films and performed AFM imaging. DD performed and analyzed the XPS data. SZ and MC performed X-ray diffraction and optical studies under irradiation. ER performed magnetic studies. CH performed EPR studies. LC analyzed the magnetic and X-ray diffraction data. EC analyzed the photoinduced X-ray diffraction and optical data. TM wrote the paper with contributions from all the authors.

Notes

The authors declare no conflict of interest.

Accepted Manuscript

ACKNOWLEDGEMENTS

We thank the Université Paris-Saclay, the CNRS (Centre National de la Recherche Scientifique), the French program ANR (project ANR-13-BS04-0002-03) for financial support. TM and LC thank the IUF for financial support. LT thanks the Vietnamese government for Scholarship, thesis code MN31.

Keywords

nanocrystals; photomagnetic; Prussian blue analogue; matrix effect; relaxation

TOC

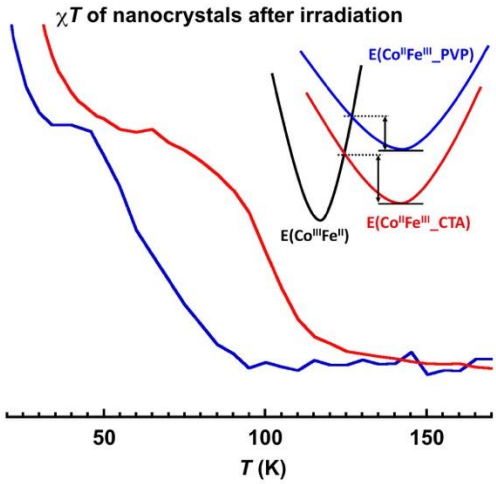

Synergy between chemical environment and size is a unique way to control the relaxation temperature of the photoinduced state in ultra-small -11 nm- CsCoFe Prussian blue analogue photo-switchable nanocrystals.

REFERENCES

1. Ferlay, S.; Mallah, T.; Ouahes, R.; Veillet, P.; Verdaguer, M., A Room-Temperature Organometallic Magnet Based on Prussian Blue. *Nature* **1995,** *378* (6558), 701-703.
2. Sato, O.; Iyoda, T.; Fujishima, A.; Hashimoto, K., Photoinduced magnetization of a cobalt-iron cyanide. *Science* **1996,** *272* (5262), 704-705.
3. Tokoro, H.; Ohkoshi, S.; Matsuda, T.; Hashimoto, K., A large thermal hysteresis loop produced by a charge-transfer phase transition in a rubidium manganese hexacyanoferrate. *Inorg. Chem.* **2004,** *43* (17), 5231-5236.
4. Mahfoud, T.; Molnar, G.; Bonhommeau, S.; Cobo, S.; Salmon, L.; Demont, P.; Tokoro, H.; Ohkoshi, S. I.; Boukheddaden, K.; Bousseksou, A., Electric-Field-Induced Charge-Transfer Phase Transition: A Promising Approach Toward Electrically Switchable Devices. *J. Am. Chem. Soc.* **2009,** *131* (41), 15049-15054.
5. Aguila, D.; Prado, Y.; Koumousi, E. S.; Mathoniere, C.; Clerac, R., Switchable Fe/Co Prussian blue networks and molecular analogues. *Chem. Soc. Rev.* **2016,** *45* (1), 203-224.

Accepted Manuscript

6. Ohkoshi, S.; Nakagawa, K.; Imoto, K.; Tokoro, H.; Shibata, Y.; Okamoto, K.; Miyamoto, Y.; Komine, M.; Yoshikiyo, M.; Namai, A., A photoswitchable polar crystal that exhibits superionic conduction. *Nat. Chem.* **2020**.
7. Okubo, M.; Li, C. H.; Talham, D. R., High rate sodium ion insertion into core-shell nanoparticles of Prussian blue analogues. *Chem. Commun.* **2014,** *50* (11), 1353-1355.
8. Hurlbutt, K.; Wheeler, S.; Capone, I.; Pasta, M., Prussian Blue Analogs as Battery Materials. *Joule* **2018,** *2* (10), 1950-1960.
9. Pintado, S.; Goberna-Ferron, S.; Escudero-Adan, E. C.; Galan-Mascaros, J. R., Fast and Persistent Electrocatalytic Water Oxidation by Co-Fe Prussian Blue Coordination Polymers. *J. Am. Chem. Soc.* **2013,** *135* (36), 13270-13273.
10. Goberna-Ferron, S.; Hernandez, W. Y.; Rodriguez-Garcia, B.; Galan-Mascaros, J. R., Light-Driven Water Oxidation with Metal Hexacyanometallate Heterogeneous Catalysts. *ACS Catal.* **2014,** *4* (6), 1637-1641.
11. Cai, X. J.; Gao, W.; Zhang, L. L.; Ma, M.; Liu, T. Z.; Du, W. X.; Zheng, Y. Y.; Chen, H. R.; Shi, J. L., Enabling Prussian Blue with Tunable Localized Surface Plasmon Resonances: Simultaneously Enhanced Dual-Mode Imaging and Tumor Photothermal Therapy. *Acs Nano* **2016,** *10* (12), 11115-11126.
12. Patra, C. R., Prussian blue nanoparticles and their analogues for application to cancer theranostics. *Nanomedicine* **2016,** *11* (6), 569-572.
13. Fetiveau, L.; Paul, G.; Nicolas-Boluda, A.; Volatron, J.; George, R.; Laurent, S.; Muller, R.; Sancey, L.; Mejanelle, P.; Gloter, A.; Gazeau, F.; Catala, L., Tailored ultra-small Prussian blue-based nanoparticles for MRI imaging and combined photothermal/photoacoustic theranostics. *Chem. Commun.* **2019,** *55* (98), 14844-14847.
14. Assis, L. M. N.; Leones, R.; Kanicki, J.; Pawlicka, A.; Silva, M. M., Prussian blue for electrochromic devices. *J. Electroanal. Chem.* **2016,** *777*, 33-39.
15. Catala, L.; Mallah, T., Nanoparticles of Prussian blue analogs and related coordination polymers: From information storage to biomedical applications. *Coord. Chem. Rev.* **2017,** *346*, 32-61.
16. Moulin, C. C. D.; Villain, F.; Bleuzen, A.; Arrio, M. A.; Sainctavit, P.; Lomenech, C.; Escax, V.; Baudelet, F.; Dartyge, E.; Gallet, J. J.; Verdaguer, M., Photoinduced ferrimagnetic systems in Prussian blue analogues C-x(I)Co-4[Fe(CN)(6)](y) (C-I = alkali cation). 2. X-ray absorption spectroscopy of the metastable state. *J. Am. Chem. Soc.* **2000,** *122* (28), 6653-6658.
17. Champion, G.; Escax, V.; Moulin, C. C. D.; Bleuzen, A.; Villain, F. O.; Baudelet, F.; Dartyge, E.; Verdaguer, N., Photoinduced ferrimagnetic systems in prussian blue analogues (CxCo4)-Co-I[Fe(CN)(6)](y) (C-I = alkali cation). 4. Characterization of the ferrimagnetism of the photoinduced metastable state in Rb1.8Co4[Fe(CN)(6)](3.3)center dot 13H(2)O by K edges X-ray magnetic circular dichroism. *J. Am. Chem. Soc.* **2001,** *123* (50), 12544-12546.
18. Escax, V.; Bleuzen, A.; Moulin, C. C. D.; Villain, F.; Goujon, A.; Varret, F.; Verdaguer, M., Photoinduced ferrimagnetic systems in prussian blue analogues (CxCo4)-Co-I[Fe(CN)(6)](y) (C-I = alkali cation). 3. Control of the photo- and thermally induced electron transfer by the [Fe(CN)(6)] vacancies in cesium derivatives. *J. Am. Chem. Soc.* **2001,** *123* (50), 12536-12543.
19. Escax, V.; Champion, G.; Arrio, M. A.; Zacchigna, M.; Moulin, C. C. D.; Bleuzen, A., The Co ligand field: A key parameter in photomagnetic CoFe Prussian blue derivatives. *Angew. Chem. Int. Ed.* **2005,** *44* (30), 4798-4801.
20. Han, L. J.; Tang, P. Y.; Reyes-Carmona, A.; Rodriguez-Garcia, B.; Torrens, M.; Morante, J. R.; Arbiol, J.; Galan-Mascaros, J. R., Enhanced Activity and Acid pH Stability of Prussian Blue-type Oxygen Evolution Electrocatalysts Processed by Chemical Etching. *J. Am. Chem. Soc.* **2016,** *138* (49), 16037-16045.

Accepted Manuscript

21. Moore, J. G.; Lochner, E. J.; Ramsey, C.; Dalal, N. S.; Stiegman, A. E., Transparent, superparamagnetic K(x)(I)Coy(II)[Fe-III(CN)(6)]1 - Silica nanocomposites with tunable photomagnetism. *Angew. Chem. Int. Ed.* **2003,** *42* (24), 2741-2743.
22. Pajerowski, D. M.; Frye, F. A.; Talham, D. R.; Meisel, M. W., Size dependence of the photoinduced magnetism and long-range ordering in Prussian blue analogue nanoparticles of rubidium cobalt hexacyanoferrate. *New J. Phys.* **2007,** *9*.
23. Mouawia, R.; Larionova, J.; Guari, Y.; Oh, S.; Cook, P.; Prouzet, E., Synthesis of Co-3[Fe(CN)(6)](2) molecular-based nanomagnets in MSU mesoporous silica by integrative chemistry. *New J. Chem.* **2009,** *33* (12), 2449-2456.
24. Moulin, R.; Delahaye, E.; Bordage, A.; Fonda, E.; Baltaze, J. P.; Beaunier, P.; Riviere, E.; Fornasieri, G.; Bleuzen, A., Ordered Mesoporous Silica Monoliths as a Versatile Platform for the Study of Magnetic and Photomagnetic Prussian Blue Analogue Nanoparticles. *Eur. J. Inorg. Chem.* **2017,** (10), 1303-1313.
25. Fornasieri, G.; Bordage, A.; Bleuzen, A., Magnetism and Photomagnetism of Prussian Blue Analogue Nanoparticles Embedded in Porous Metal Oxide Ordered Nanostructures. *Eur. J. Inorg. Chem.* **2018,** (3-4), 259-271.
26. Tokoro, H.; Ohkoshi, S., Multifunctional Material: Bistable Metal-Cyanide Polymer of Rubidium Manganese Hexacyanoferrate. *Bull. Chem. Soc. Jpn.* **2015,** *88* (2), 227-239.
27. Zerdane, S.; Cammarata, M.; Balducci, L.; Bertoni, R.; Catala, L.; Mazerat, S.; Mallah, T.; Pedersen, M. N.; Wulff, M.; Nakagawa, K.; Tokoro, H.; Ohkoshi, S.; Collet, E., Probing Transient Photoinduced Charge Transfer in Prussian Blue Analogues with Time-Resolved XANES and Optical Spectroscopy. *Eur. J. Inorg. Chem.* **2018,** (3-4), 272-277.
28. Brinzei, D.; Catala, L.; Louvain, N.; Rogez, G.; Stephan, O.; Gloter, A.; Mallah, T., Spontaneous stabilization and isolation of dispersible bimetallic coordination nanoparticles of CsxNi[Cr(CN)(6)](y). *J. Mater. Chem.* **2006,** *16* (26), 2593-2599.
29. Catala, L.; Brinzei, D.; Prado, Y.; Gloter, A.; Stephan, O.; Rogez, G.; Mallah, T., Core-Multishell Magnetic Coordination Nanoparticles: Toward Multifunctionality on the Nanoscale. *Angew. Chem. Int. Ed.* **2009,** *48* (1), 183-187.
30. Prado, Y.; Mazerat, S.; Riviere, E.; Rogez, G.; Gloter, A.; Stephan, O.; Catala, L.; Mallah, T., Magnetization Reversal in (CsNiCrIII)-Cr-II(CN)(6) Coordination Nanoparticles: Unravelling Surface Anisotropy and Dipolar Interaction Effects. *Adv. Funct. Mater.* **2014,** *24* (34), 5402-5411.
31. Felts, A. C.; Andrus, M. J.; Averback, C. M.; Li, C. H.; Talham, D. R., Comparison of the infrared absorptivities of some Prussian blue analogues and their use to determine the composition of core-shell particles. *Polyhedron* **2017,** *133*, 404-411.
32. Powell, C. J.; Jablonski, A., Evaluation of calculated and measured electron inelastic mean free paths near solid surfaces. *J. Phys. Chem. Ref. Data* **1999,** *28* (1), 19-62.
33. Tanuma, S.; Powell, C. J.; Penn, D. R., Calculation of electron inelastic mean free paths (IMFPs) VII. Reliability of the TPP-2M IMFP predictive equation. *Surf. Interface Anal.* **2003,** *35* (3), 268-275.
34. Bordage, A.; Moulin, R.; Fonda, E.; Fornasieri, G.; Riviere, E.; Bleuzen, A., Evidence of the Core-Shell Structure of (Photo)magnetic CoFe Prussian Blue Analogue Nanoparticles and Peculiar Behavior of the Surface Species. *J. Am. Chem. Soc.* **2018,** *140* (32), 10332-10343.
35. Ohlin, C. A.; Harley, S. J.; McAlpin, J. G.; Hocking, R. K.; Mercado, B. Q.; Johnson, R. L.; Villa, E. M.; Fidler, M. K.; Olmstead, M. M.; Spiccia, L.; Britt, R. D.; Casey, W. H., Rates of Water Exchange for Two Cobalt(II) Heteropolyoxotungstate Compounds in Aqueous Solution. *Chem. Eur. J.* **2011,** *17* (16), 4408-4417.
36. Kuhlman, M. L.; Rauchfuss, T. B., Structural chemistry of "defect" cyanometalate boxes: {Cs subset of[CpCo(CN)(3)](4)[Cp*Ru](3)} and {M subset of[Cp*Rh(CN)(3)](4)[Cp*Ru](3)} (M = NH4, Cs). *J. Am. Chem. Soc.* **2003,** *125* (33), 10084-10092.

Accepted Manuscript

37. Jimenez, J. R.; Tricoire, M.; Garnier, D.; Chamoreau, L. M.; von Bardeleben, J.; Journaux, Y.; Li, Y. L.; Lescouezec, R., A new {Fe4Co4} soluble switchable nanomagnet encapsulating Cs+: enhancing the stability and redox flexibility and tuning the photomagnetic effect. *Dalton Trans.* **2017,** *46* (44), 15549-15557.
38. Bleuzen, A.; Escax, V.; Ferrier, A.; Villain, F.; Verdaguer, M.; Munsch, P.; Itie, J. P., Thermally induced electron transfer in a CsCoFe Prussian blue derivative: The specific role of the alkali-metal ion. *Angew. Chem. Int. Ed.* **2004,** *43* (28), 3728-3731.
39. Raza, Y.; Volatron, F.; Moldovan, S.; Ersen, O.; Huc, V.; Martini, C.; Brisset, F.; Gloter, A.; Stephan, O.; Bousseksou, A.; Catala, L.; Mallah, T., Matrix-dependent cooperativity in spin crossover Fe(pyrazine)Pt(CN)(4) nanoparticles. *Chem. Commun.* **2011,** *47* (41), 11501-11503.
40. Tissot, A.; Enachescu, C.; Boillot, M. L., Control of the thermal hysteresis of the prototypal spin-transition Fe-II(phen)(2)(NCS)(2) compound via the microcrystallites environment: experiments and mechanoelastic model. *J. Mater. Chem.* **2012,** *22* (38), 20451-20457.
41. Enachescu, C.; Tanasa, R.; Stancu, A.; Tissot, A.; Laisney, J.; Boillot, M. L., Matrix-assisted relaxation in Fe(phen)(2)(NCS)(2) spin-crossover microparticles, experimental and theoretical investigations. *Appl. Phys. Lett.* **2016,** *109* (3).
42. Tanasa, R.; Enachescu, C.; Laisney, J.; Morineau, D.; Stancu, A.; Boillot, M. L., Unraveling the Environment Influence in Bistable Spin-Crossover Particles Using Magnetometric and Calorimetric First-Order Reverse Curves. *J. Phys. Chem. C* **2019,** *123* (15), 10120-10129.
43. Kawamoto, T.; Asai, Y.; Abe, S., Ab initio calculations on the mechanism of charge transfer in Co-Fe Prussian-blue compounds. *Phys. Rev. B* **1999,** *60* (18), 12990-12993.
44. Coronado, E.; Forment-Aliaga, A.; Pinilla-Cienfuegos, E.; Tatay, S.; Catala, L.; Plaza, J. A., Nanopatterning of Anionic Nanoparticles based on Magnetic Prussian-Blue Analogues. *Adv. Funct. Mater.* **2012,** *22* (17), 3625-3633.
45. Pinilla-Cienfuegos, E.; Kumar, S.; Manas-Valero, S.; Canet-Ferrer, J.; Catala, L.; Mallah, T.; Forment-Aliaga, A.; Coronado, E., Imaging the Magnetic Reversal of Isolated and Organized Molecular-Based Nanoparticles using Magnetic Force Microscopy. *Part. Part. Syst. Charac.* **2015,** *32* (6), 693-700.

Accepted Manuscript

Supporting Information

Photo-Switchable 11 nm CsCoFe Prussian Blue Analogue Nanocrystals with High Relaxation Temperature

*Linh Trinh, Serhane Zerdane, Sandra Mazérat, Nada Dia, Diana Dragoe, Christian Herrero, Eric Rivière, Laure Catala, Marco Cammarata, Eric Collet, Talal Mallah**

Dr. L. Trinh, S. Mazérat, N. Dia, Dr. D. Dragoe, Dr. C. Herrero, Dr. E. Rivière
Prof. L. Catala, Prof. T. Mallah
Institut de Chimie Moléculaire et des Matériaux d'Orsay
Université Paris-Saclay, CNRS
15, rue Georges Clémenceau
91405, Orsay Cedex, France
e-mail : talal.mallah@universite-paris-saclay.fr, talal.mallah@u-psud.fr

Dr. S. Zerdane, Dr. M. Cammarata, Prof. E. Collet
Univ Rennes 1, CNRS
IPR (Institut de Physique de Rennes), UMR 6251
F-35042 Rennes, France

Accepted Manuscript

1. Experimental

The TEM measurements have been done on a TEM Philips EM208 with 100 keV incident electrons focused on the specimen.
The Dynamic light scattering measurement has been performed on a Malvern Nanozetasizer Apparatus (equipped with a backscattering mode) on the aqueous solutions containing the particles. The volume profile was used to estimate the size corresponding to the main peaks. This measurement was used as a qualitative measurement of the size of the particles or aggregates in solution, which systematically includes a solvation shell.
FT-IR spectra were recorded with a PerkinElmer spectrometer (Spectrum 100). The measurements were performed on KBr pellets (typically 1 mg in ca. 99 mg of KBr, this latter being previously ground) in the 300−4000 cm^{-1} range.
Powder X-ray diffraction (XRD) was performed on powders deposited on an aluminum plate and collected on a Philipps Panalytical X'Pert Pro MPD powder diffractometer at CuKα radiation equipped with a fast detector.
XPS measurements were performed on a K Alpha spectrometer from ThermoFisher, equipped with a monochromated X-ray Source (Al K_α, 1486.6 eV) using a spot size of 400 µm. The hemispherical analyser was operated in CAE (Constant Analyser Energy) mode, with a pass energy of 200 eV and a step of 1 eV for the acquisition of surveys spectra, and a pass energy of 50 eV and a step of 0.1 eV for the acquisition of narrow spectra. The spectra obtained were treated by means of the Avantage software. A Shirley type background subtraction was used and the peak areas were normalized using the Scofield sensitivity factors. The peaks were analyzed using mixed Gaussian-Lorentzian curves (70% of Gaussian character). The binding energies were calibrated against the C1s binding energy of graphitic carbon set at 284.6 eV.
X-band EPR spectra were recorded on a Bruker ELEXSYS 500 spectrometer equipped with a Bruker ER 4116DM X band resonator, an Oxford Instrument continuous flow ESR 900 cryostat, and an Oxford ITC 503 temperature control system. The aqueous dispersion containing the nanoparticles (200 µL) was transferred to an EPR tube and frozen to 77 K prior to insertion in the EPR apparatus. For *in situ* sample illuminations, we used a Thorlabs high power LED operating at 635 nm aimed directly at the

EPR resonator. The samples were illuminated directly in the cavity at different temperatures and for different time periods prior to EPR measurement (See figure legends for details). The standard experimental conditions are: microwave frequency 9.63 GHz, microwave power 1.0 mW, modulation amplitude 8 Gauss, modulation frequency 100 KHz, gain 34 dB.
Magnetic measurements were carried out with a Quantum Design MPMS-5S magnetometer working in the dc mode. Photomagnetic experiments were carried out on the same magnetometer that was equipped with a UV-Vis optical fiber connected to a 635nm Laser diode. The samples were deposited and pressed between two pieces of adhesive tape to form a thin film to avoid any orientation of the powder with the magnetic field and to maximize light penetration during the irradiation process. 0.4 mg were used for the CsCoFe_CTA sample and 3.8 mg for the CsCoFe_PVP one.

2. Preparation of the nanoparticles

CsCoFe_CTA (1). 200 ml of distilled water containing 673 mg of CsCl (4 mM) and 476 mg (2 mM) of $[Co^{II}(H_2O)_6]Cl_2$ were quickly added to 200 ml of distilled water containing 658 mg (2 mM) of $K_3[Fe^{III}(CN)_6]$. The solution was vigorously mixed for 30 minutes. DLS was measured (Figure S1).
A methanolic solution (600 ml) containing 1.10 g (6 mM) of cetyltrimethylammonium bromide (CTABr) is prepared and added dropwise to 200 ml (half) of the aqueous solution containing the nanoparticles. A precipitate form during the addition, it is recovered by centrifugation (9000 rpm for 20 minutes) washed with a small amount of water and dried under vacuum overnight. Elemental analysis for $Cs_{0.7}(C_{19}H_{42}N)_{0.4}Co[Fe(CN)_6]_{0.9}(H_2O)_{0.6}$, exp. (calc.) C: 20.10 (20.60), H: 2.43 (3.79), N: 17.70 (17.12). For Cs, Fe and Co see Table S1.
CsCoFe_PVP (2). The remaining 200 ml of the nanoparticles is added dropwise for 3 hours to 20 ml of an aqueous solution containing 12 g of PVP. Then 900 ml of acetone is added to the nanoparticles dispersion. A precipitate form, it is recovered by centrifugation (9000 rpm for 20 minutes) washed with a small amount of acetone and dried under vacuum overnight. EDS see Table S1.
Cs_2CoFe (3). 50 ml of distilled water containing CsCl (10mM) and $[Co^{II}(H_2O)_6]Cl_2$ (5mM) was added drop-wise to a 50 ml aqueous solution of $K_4[Fe^{II}(CN)_6]\bullet 2H_2O$ (5mM) using a peristaltic pump (1.5 ml/minutes) while stirring vigorously. Upon adding, a suspension with a brown yellow color formed. The compound was collected using centrifugation (9000 rpm, 20 minutes) and washed one time with distilled water and one time with acetone and then dried under vacuum. EDS, see Table S1; $Cs_2[Co^{II}\{Fe^{II}(CN)_6\}]\bullet 2H_2O$ Elemental analysis: exp. (calc.) C: 12.35 (12.40), H: 0.73 (0.69), N: 14.62 (14.46)
$CoFe_{0.66}$ (4). 50 ml of an aqueous solution containing $CoCl_2\bullet 6H_2O$ (2 mM, 23.8 mg) was added to 50 ml of an aqueous solution containing $K_3[Fe^{III}(CN)_6]$ (2 mM, 32.9 mg). The solution was then stirred vigorously for 60 hours. The mixture changed color from colorless to dark orange in a few seconds then to deep red color and remains in this color for the rest of the experiment. The compound was collected using centrifugation (9000 rpm, 20 minutes) and washed one time with distilled water and one time with acetone and then dried under vacuum. EDS, see Table S1, $Co^{II}\{Fe^{III}(CN)_6\}_{0.66}\bullet 4.5H_2O$ Elemental analysis: exp. (calc.) C: 17.03 (16.99), H: 3.18 (3.21), N: 19.74 (19.82)

3. Electron Dispersive Spectroscopy

Table S1. EDS results for **1**, **2**, **3** and **4**

EDS	Co	Fe	Cs	K
sample 1	1.00	0.89	0.70	0.01
sample 2*	1.00	1.00	1.20	–
sample 3	1.00	1.00	1.80	0.02
sample 4	1.00	0.66	0.00	0.03

* the excess Fe and Cs in comparison to sample **1** is due to the ions (Cs^+, Cl^-, $Fe(CN)_6^{3-}$) present in solution that are recovered by PVP in the same time as the NPs.

Accepted Manuscript

4. Dynamic Light Scattering (DLS) studies

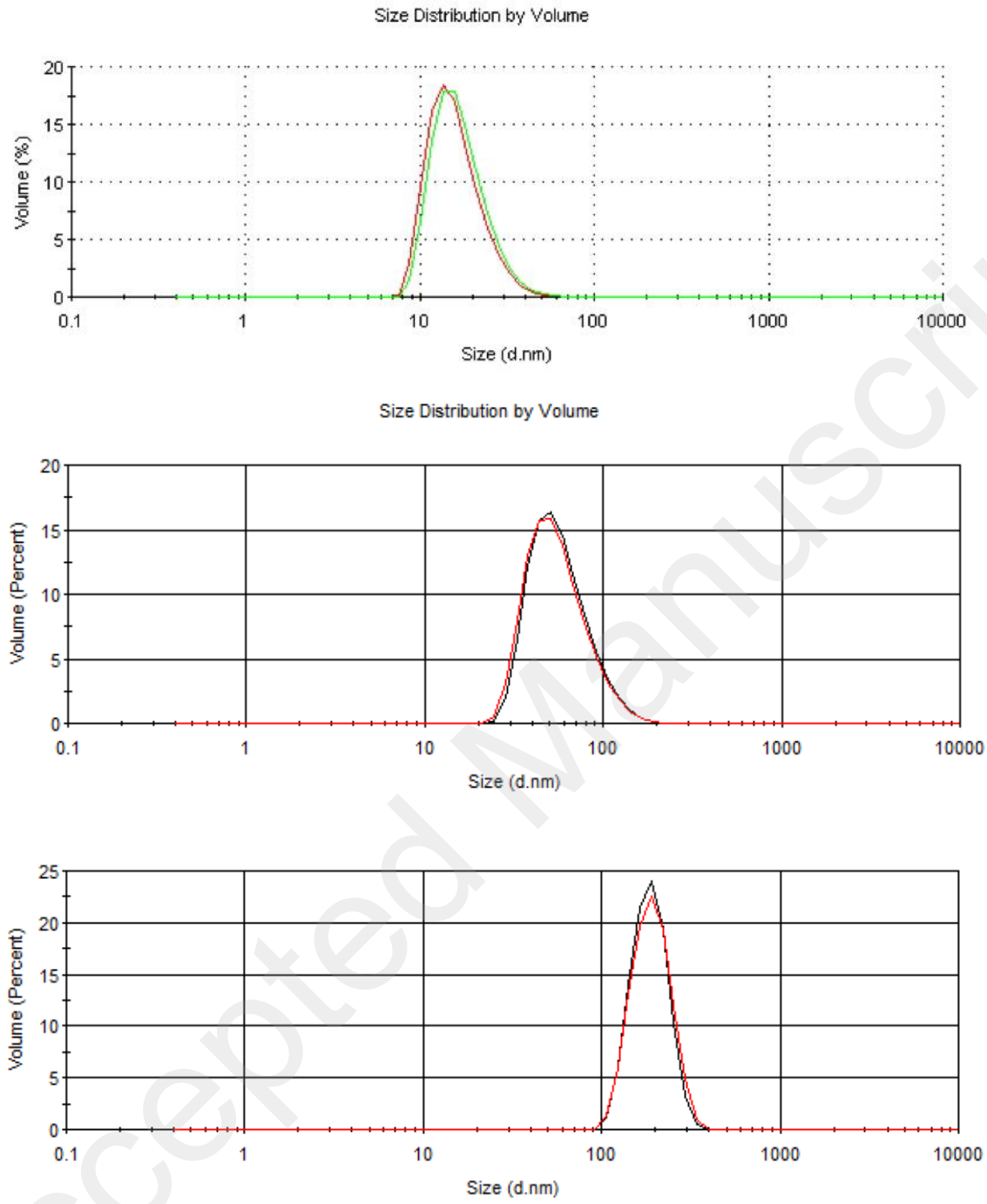

Figure S1. Dynamic Light Scattering plots for the as prepared nanoparticles: CsCoFe (top), $Cs_2Co^{II}Fe^{II}$ (middle) and $Co^{II}Fe^{III}_{0.66}$ (bottom).

Accepted Manuscript

5. Thermo Gravimetric Analysis (TGA) and Differential Scanning Calorimetry (DSC) for **1**.

In order to determine accurately the amount of water molecules, we carried a TGA study on **1**. The data show a continuous loss of matter from room temperature up to 180 °C that corresponds to 2.25% of its weight (green line) and then an intake of the same amount upon cooling down to room temperature. This weight loss amounts to 0.6 H_2O considering the formula $Cs_{0.7}(C_{19}H_{42}N)_{0.4}Co[Fe(CN)_6]_{0.9}(H_2O)_{0.6}$ (Mw = 467.02 g/mol). The DSC (dark red) shows an endothermic behavior consistent with the loss of water molecules.

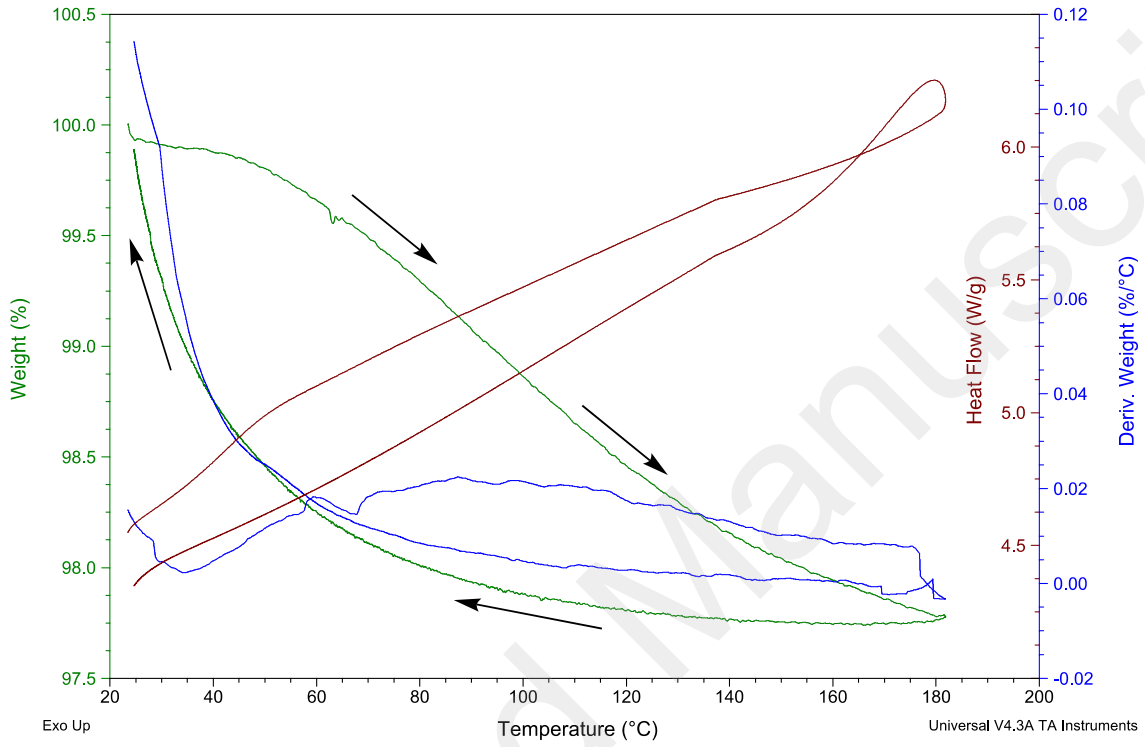

Figure S2. TGA and DSC study for **1**, weight loss (green)

Accepted Manuscript

6. Infra-red spectroscopy

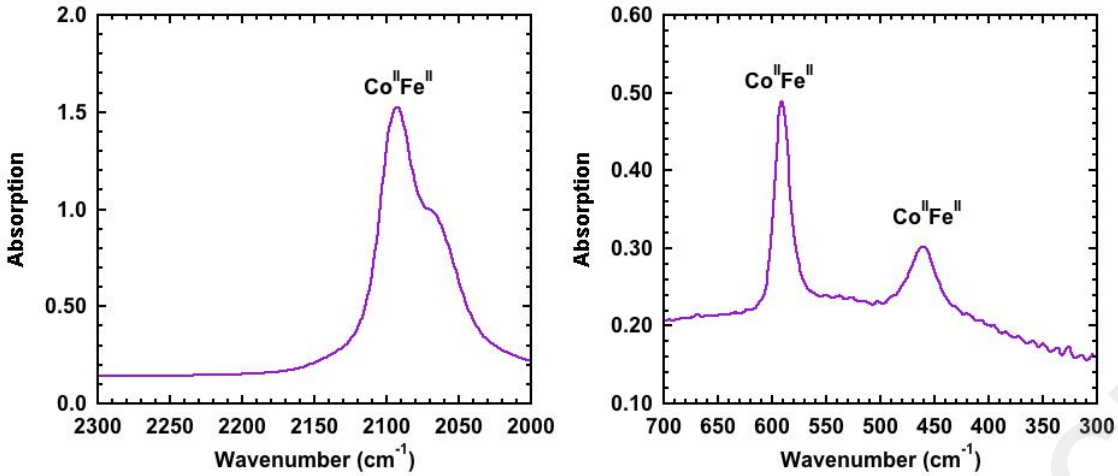

Figure S3. Infra-red spectra of Cs_2CoFe (**3**) in the 2000-2300 cm^{-1} region (left) and 300-700 cm^{-1} region (right).

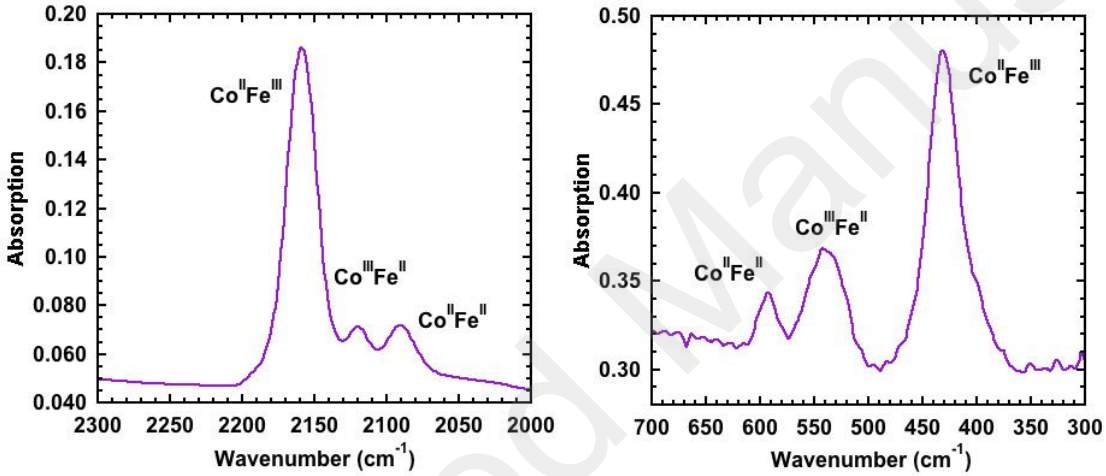

Figure S4. Infra-red spectra of $CoFe_{0.66}$ (**4**) in the 2000-2300 cm^{-1} region (left) and 300-700 cm^{-1} region (right).

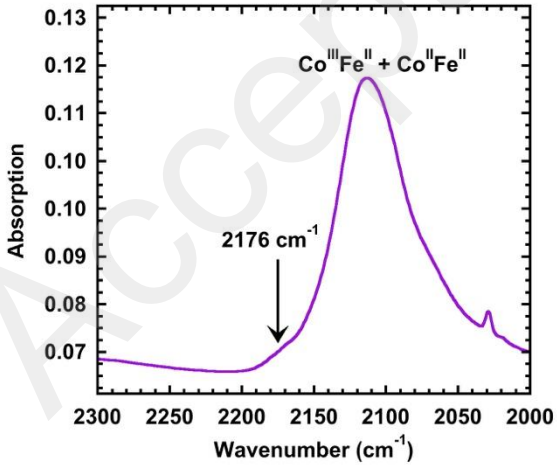

Figure S5. Infra-red spectra of CsCoFe_CTA (**1**) in the 2000-2300 cm^{-1} region.

Accepted Manuscript

7. X-ray powder diffraction (XRPD) studies

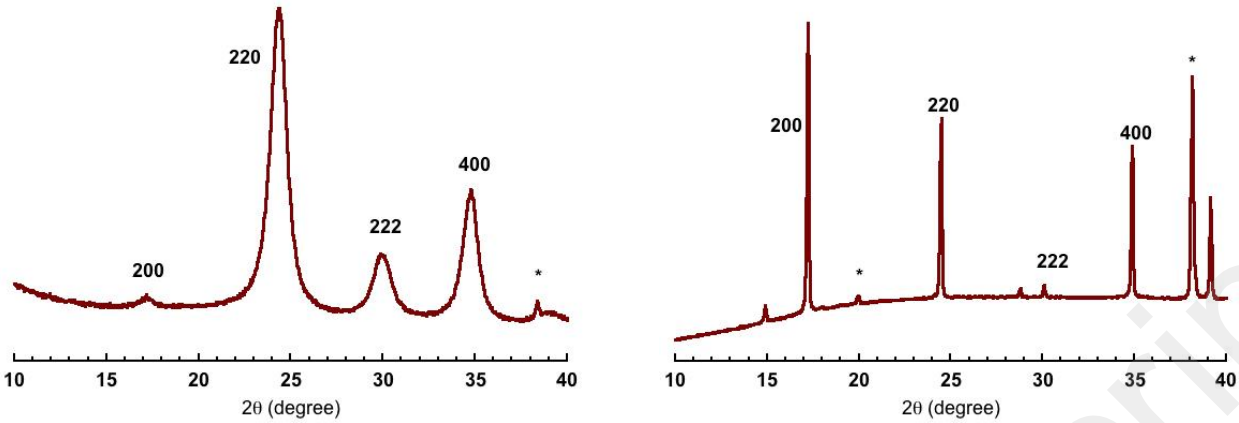

Figure S6. X-ray powder diffraction pattern for Cs_2CoFe (**3**) (left) and $CoFe_{0.66}$ (**4**) (right), the * corresponds to a Bragg peak belonging to the substrate.

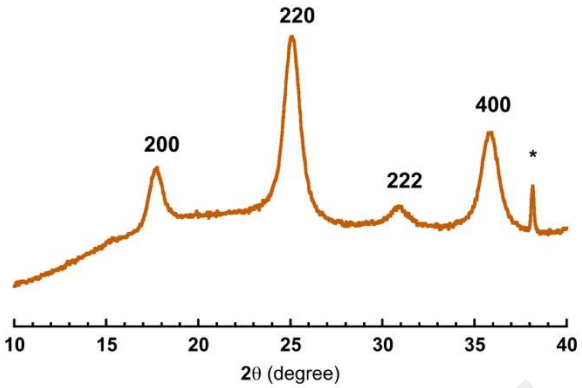

Figure S7. XRPD pattern of CsCoFe_CTA (**1**), the * corresponds to a Bragg peak belonging to the substrate.

Accepted Manuscript

8. Preparation of the nanocrystals' thin film and Atomic Force Microscopy (AFM) imaging

A freshly cleaved HOPG substrate was immersed for 15 minutes in a freshly prepared aqueous colloidal dispersion of the nanocrystals. The substrate was removed from the solution, rinsed with water and methanol then dried under a flow of argon for two hours. It was then imaged by AFM.

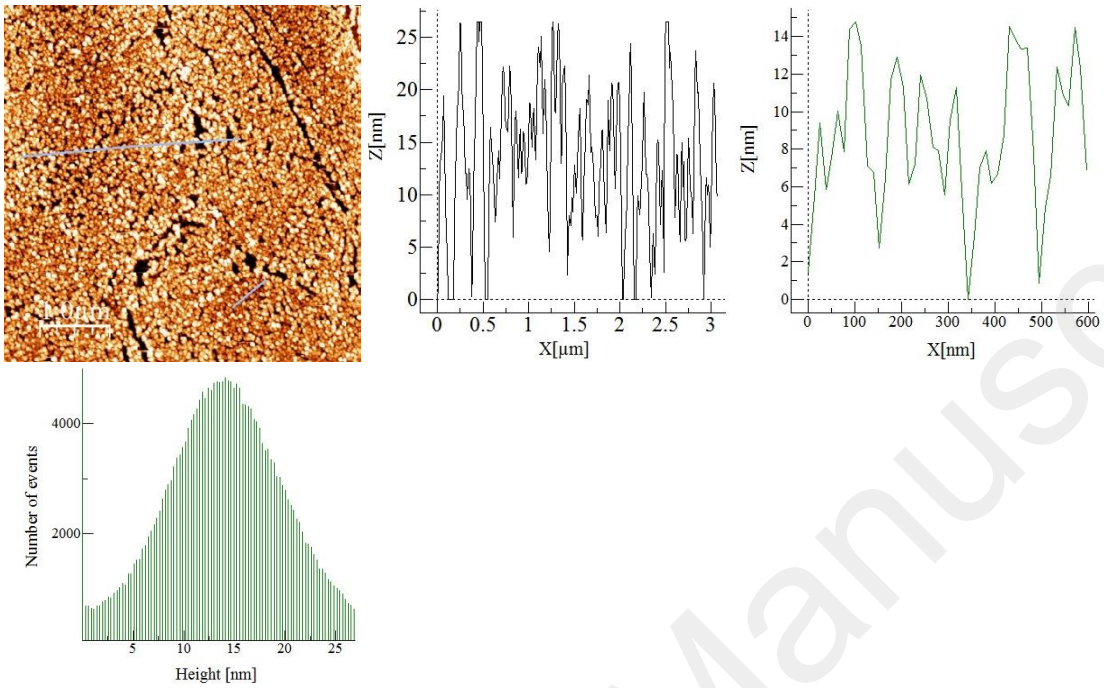

Figure S8. Atomic Force Microscopy image (5µm x 5µm) of an assembly of the CsCoFe nanocrystals on HOPG and height for two selected regions of the image and the number of events vs. height showing an average value close to 12 nm.

9. X-ray Photoelectron Spectroscopy (XPS) study

The Co2p signal is interfered by an iron Auger LMM. In order to do the correction for the Auger LMM a reference sample of K4[Fe4(CN)6] was measured and the Auger signal was subtracted from Co2p after normalizing its intensity on Fe2p peaks of the sample and that of K4[Fe4(CN)6]. It is worth mentioning that this Auger subtraction represents a source of error.

The Co2p core level spectra were recorded within a period of 10 - 41 minutes from the beginning of the acquisition. We noticed a slight modification of the Co2p signal during the exposure to X-rays beam corresponding to a reduction of Co(III) to Co(II), but the effect observed is almost negligible. In order to estimate this effect, we evaluated the Co(III)/Co(II) ratios at different exposure times which are varying from 2 after 11 min to 1.4 after 41 min as shown Figure S9.

The $Cs3d_{5/2}$ is interfered by $Fe2p_{1/2}$. As a consequence, we considered only the $Cs3d_{3/2}$ and $Fe2p_{3/2}$ areas in the quantification.

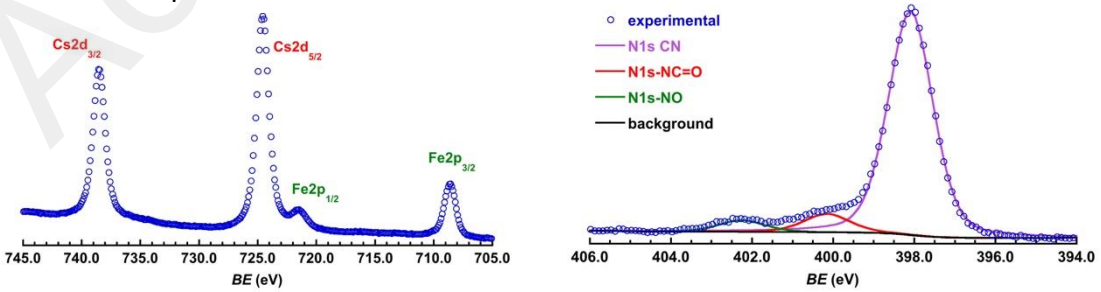

Figure S9. X-ray Photoelectron Spectroscopy spectra for the as prepared nanoparticles at the Fe and Cs edges (left) and at the N edge (right).

Accepted Manuscript

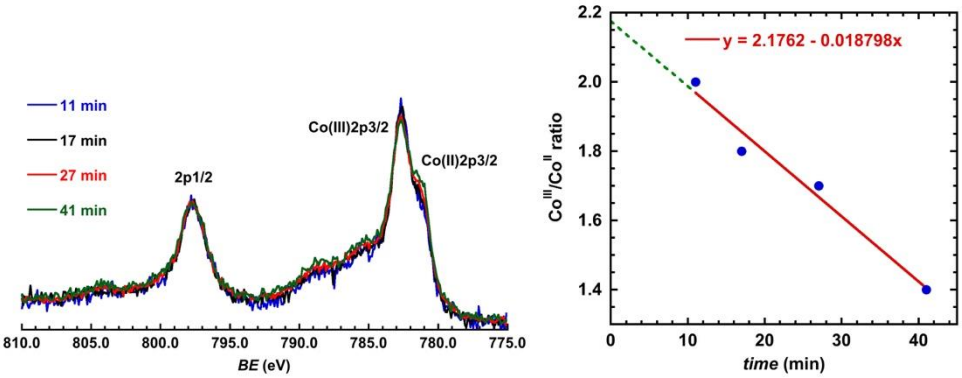

Figure S10. (left) XPS spectrum at the 2p edge of Co for the as prepared nanoparticles assembled on a HOPG at t = 11, 17, 27 and 41 minutes and (right) evolution of the Co^{III}/Co^{II} ratio with time.

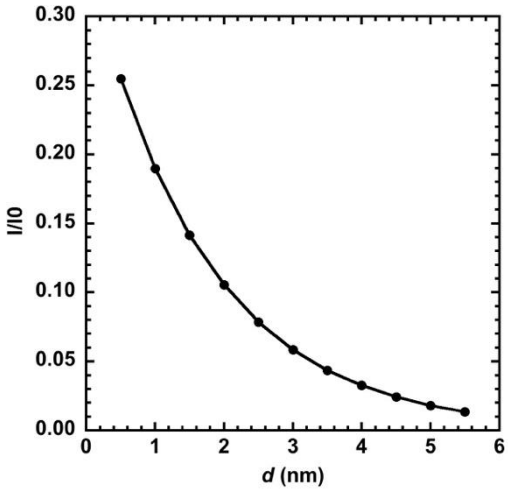

Figure S11. Variation of the intensity of the XPS spectrum as a function of the depth form the surface, *d*.

10. Determination of the contribution of the different layers for a cfc cubic nanocrystal

For a cfc cubic nanocrystal with a side of *n* nm, the overall number of metallic ions of the same nature (Fe or Co) is given by $4(n+0.5)^3 +0.5$.

A layer is defined as an atomic cube of the nanocrystal, the surface being L1, the next inner atomic cube is L2 and so on as shown in the scheme below. The distance between two layers correspond to half of the unit cell. In the present case where the unit cell parameter is equal to 10.03 Å (1 nm), the distance between two layers is $\approx$ 0.5 nm.

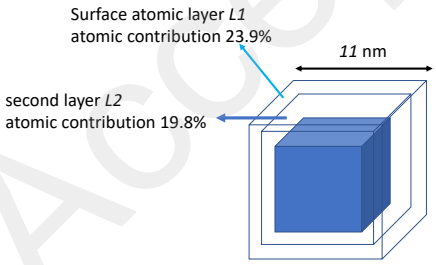

The number of atoms belonging to each layer is given by $2n^2+2n+1$. For the present case where we have nanocrystals with *n* = 11, the total number of Co (or Fe) atoms of the nanocrystal is 6084. The number of atoms belonging to the surface (L1) is 1454. For L2, we find 1202 and so on...The percentage of atoms belonging to L1 is therefore 23.9 (1454/6084) and for L2 is 19.8, etc.. Table S2 gives the number of atoms for L*n* and their percentage.

Accepted Manuscript

Table S2. Number and percentage of metallic atoms (Co or Fe) belonging to each layer L*n* of a cubic nanocrystal (fcc structure) with a side *n* = 11 nm, where L*1* is defined as the surface of the nanocrystal

Ln	number of atoms belonging L*n*	% of atoms belonging to L*n*
11	4	0.000657462
10	50	0.008218277
9	110	0.01808021
8	194	0.031886917
7	302	0.049638396
6	434	0.071334648
5	590	0.096975674
4	770	0.126561473
3	974	0.160092045
2	1202	0.19756739
1	1454	0.238987508

By considering the variation of the intensity of the XPS spectrum as a function of the depth from the surface, *d* (Figure S11) and the contribution of each layer of the nanocrystal (Table S2), it is possible to find an excellent correlation between the XRPD data and the ratio of the XPS signals for a model where Co(II) ions present only in the outer 5 layers (L1 to L5) with the following the percentages to each shell 0.4, 0.4, 0.3, 0.3 and 0.2 respectively, while the inner layers (L6 to L11) do not have Co(II) but only Co(III) ions. The layers L1 to L5 have a thickness of 2 nm (4 times the distance between two layers) leading to the conclusion that the nanocrystals are made of a 2 nm thick shell (L1 to L5) containing both Co(II) and Co(III) ions and an inner core of about 7 nm containing only Co(III) ions. It is important to note that considering either a larger concentration of Co(II) ions on the surface of the objects (within L1 and L2, for example or a larger concentration of Co(II) within the core give completely different calculated ratios for the XPS signal not consistent with the experimental. It is clear that for these calculation the statistical distribution of Co(II) and Co(III) ions within the nanocrystal was set to give the ratio obtained from XRPD. It is worth noting also that the Co^{III}/Co^{II} experimental ratio obtained from XRPD is confirmed by the magnetization data, a completely different technique (see below the magnetic data section)

11. <u>X-ray powder diffraction (XRPD) studies under excitation at 660 nm at 80 K</u>

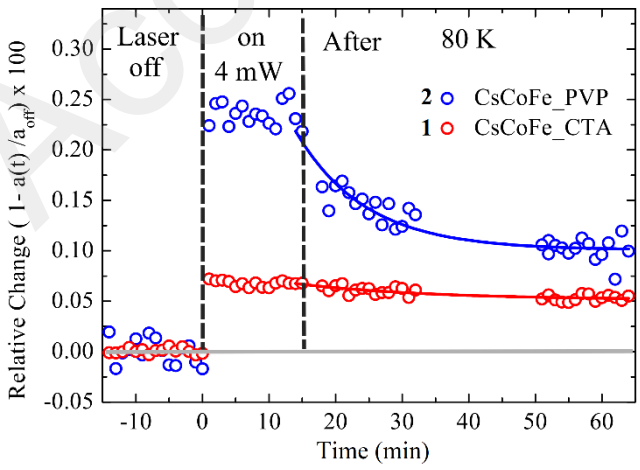

Accepted Manuscript

Figure S12. Relative lattice parameter changes of CsCoFe_CTA (**1**) and CsCoFe_PVP (**2**) under laser irradiation at 660 nm (4 mW) and at 80 K.

We performed XRD study on CsCoFe_CTA (**1**) and CsCoFe_PVP (**2**) under laser irradiation at 660 nm at 80 K (as under laser excitation at 532 nm at 10 K shown in Figure 3). Figure S12 shows the relative change of the lattice parameter $\boldsymbol{a}\left(\frac{a(t)}{a_0}-1\right)$, where a_0 is the initial lattice parameter. Under 4 mW excitation, ***a*** expends from 10.068 Å to 10.093 Å for CsCoFe_PVP (**2**), which is smaller than the expansion observed at 10 K under excitation at 532 nm (Figure 3). The expansion is weaker for CsCoFe_CTA (**1**) under 4 mW excitation at 660 nm, probably due to the larger optical density of the film which precludes high conversion. Our data collections indicate that there is no X-ray induced transformation, as the lattice parameter remains constant before laser irradiation, and only expands under laser irradiation. Once laser excitation is switched off, the lattice parameter decreases more rapidly in CsCoFe_PVP (**2**) than in CsCoFe_CTA (**1**), which indicates a stronger stabilization of the photoinduced state in CsCoFe_CTA (**1**).

12. Electron Paramagnetic Resonance (EPR) Studies

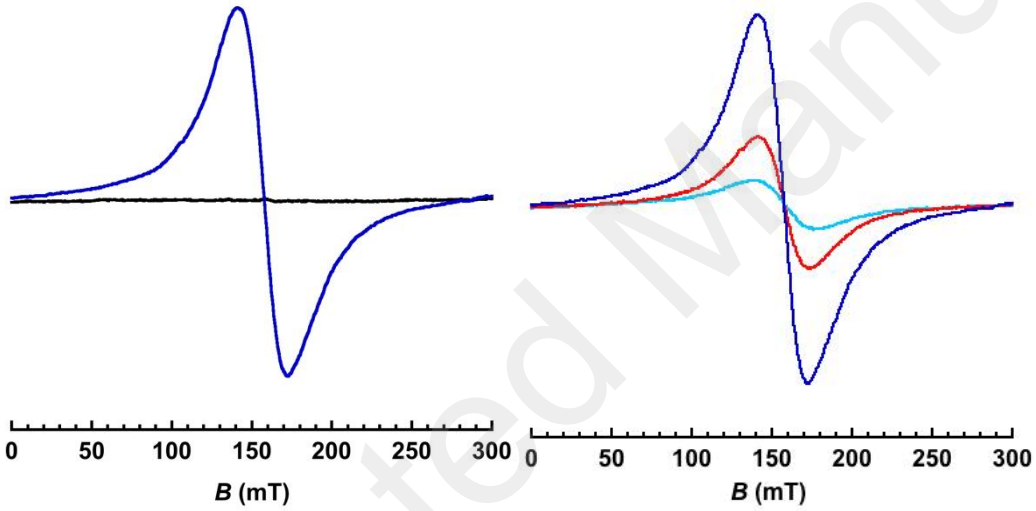

Figure S13. (left) EPR spectra for Cs_2CoFe (**3**) (blue) and $CoFe_{0.66}$ (**4**) (black) dispersed in water at T = 10 K and (right) for Cs_2CoFe (**3**) at T = 50 K (light blue), 30 K (red) and 10 K (blue). Experimental conditions (microwave frequency = 9.63 GHz, modulation amplitude = 8 G, microwave power = 1.00 mW, modulation frequency 100 KHz, gain = 34 dB).

13. Magnetic and photomagnetic studies

Magnetic behavior of $Cs_2Co^{II}Fe^{II}$ (**3**) and $Co^{II}Fe^{III}_{0.66}$ (**4**)

Upon cooling from T = 300 K, the χT = f(T) plot for $Cs_2Co^{II}Fe^{II}$ (**3**) decreases from 3.0 and reaches a value of 1.6 emuK/mol at T = 2 K (Figure S14). The value at high temperature corresponds to isolated Co^{II} ions with a g-value equal to 2.5. The shape of the curve corresponds to high spin S = 3/2 Co^{II} ions possessing relatively large spin-orbit coupling as expected for a slightly distorted octahedral geometry.[37] Because χT does not reach zero at low temperature, no large antiferromagnetic exchange coupling among the Co^{II} ions separated by diamagnetic $Fe^{II}(CN)_6$ entities is present. The overall behavior may, therefore, be attributed to a large zero-field splitting (ZFS) of the Co^{II} ions. This is consistent with the EPR data that shows an effective g-value equal to 4.1 due to transitions within the M_S = ±1/2 sub-levels well separated from the excited M_S = ±3/2, as shown by the temperature

Accepted Manuscript

dependence of the EPR spectrum (Figure S13). The magnetization vs. field (M = f(B)) measured at T = 2, 4 and 6 K (Figure S14) is almost saturated at T = 2 K and B = 6 T with a value of 2.15 Bohr Magneton well below the expected one for S = 3/2 and g = 2.5 (3.75 Bohr Magneton) consistent with a large ZFS. We also measured the thermal dependence of χT for $Co^{II}Fe^{III}_{0.66}$ (**4**). At room temperature (Figure S15), χT (3.38 emu K / mol) is slightly larger than that of $Cs_2Co^{II}Fe^{II}$ (**3**) (3.0 emu K / mol) due to the presence of 0.66 excess paramagnetic $Fe^{III}(CN)_6$ S = 1/2 species that account for 0.38 emu K / mol. Upon cooling, χT slightly decreases and reaches a value of 3.10 emu K / mol at T = 70 K indicating a weak antiferromagnetic exchange coupling between Co^{II} and Fe^{III} through the cyanide bridge. Below 70 K, χT increases to reach a maximum value of 31.50 emu K / mol at T = 12 K due to large interparticle magnetic correlation in the ferrimagnetic state. The examination of the M = f(B) curve measured at T = 2 K (Figure S15) reveals, upon increasing the field, a rather smooth increase of the magnetization that does not reach saturation at B = 5 T, whereas, the magnetization for the paramagnetic compound $Cs_2Co^{II}Fe^{II}$ (**3**) is steeper and reaches saturation. The magnetization behavior can be ascribed to the antiferromagnetic Co^{II}-Fe^{III} coupling that is weak enough so that it can be partially overcome by the relatively small applied magnetic field. Finally, no photomagnetic effect was observed confirming the absence of photoswitchable $Co^{III}Fe^{II}$ species within $Co^{II}Fe^{III}_{0.66}$ (**4**), as expected.

It is important note that we used the values of the magnetization at T = 2 K and B = 6 T to draw quantitative conclusion on the concentration of the different metal ions, and not the values of χT at high temperature where the spin-only approximation is valid. This is because the χT value above 250 K is not accurate and cannot be used to draw quantitative conclusions, this is due to the following reasons: (i) we are dealing with a sample (CsCoFe_CTA) that is mainly made of diamagnetic ions (Co(III) and Fe(II)) with only around 30% of paramagnetic Co(II), (ii) the diamagnetic contribution is large because the nanocrystals are surrounded by CTA, and (iii) we used a very small amount of matter (0.4 mg) to measure the magnetization in order to maximize light penetration and photomagnetic transformation. All these reasons make the paramagnetic signal low and the diamagnetic one large at room temperature and difficult to be exactly evaluated. A large uncertainty on the χT value above 250 K where the spin-only approximation is valid, occurs. While magnetization data at 2 K and 6 T give a large magnetic signal with relatively negligible diamagnetic one. We, therefore, rely on these values to interpret our results.

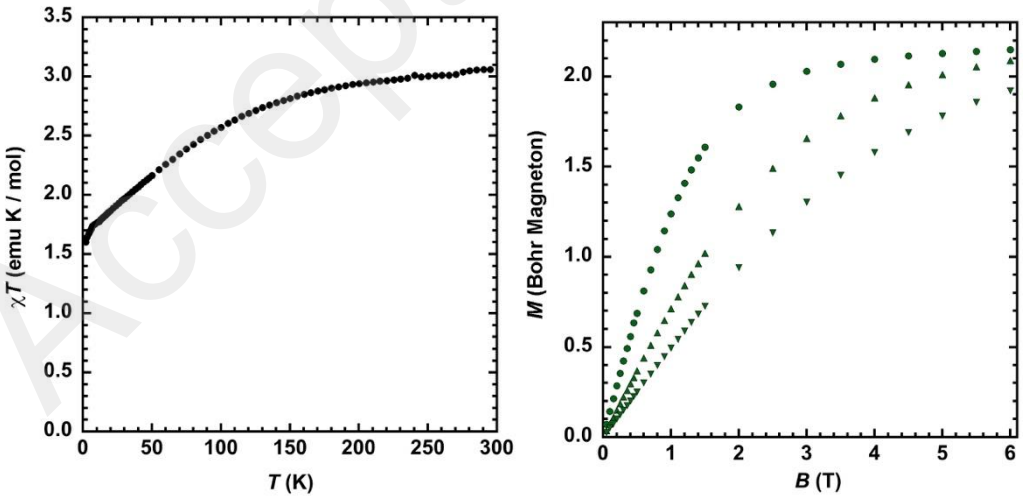

Figure S14. (left) χT = f(T) and (right) M = f(B) for Cs_2CoFe (**3**) at T = 2 K (●), 4 K (▲) and 6 K (▼).

Accepted Manuscript

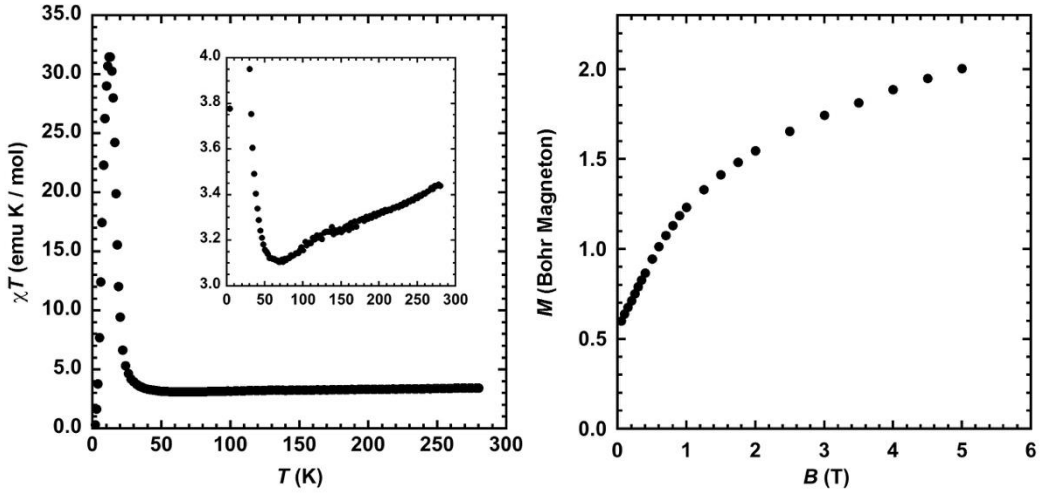

Figure S15. (left) χT = f(T) and (right) M = f(B) at T = 2 K for $CoFe_{0.66}$ (**4**).

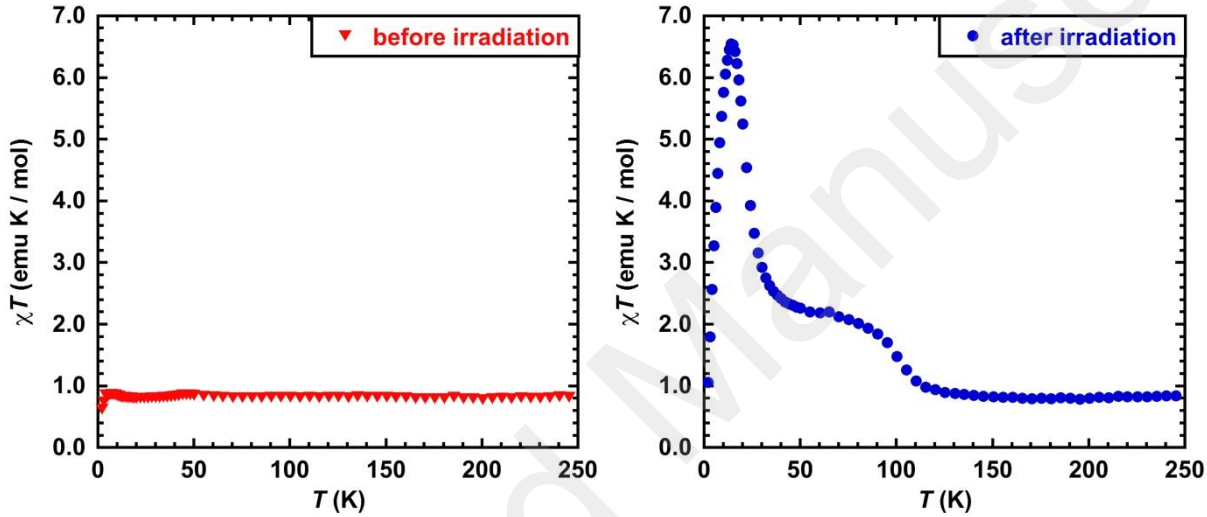

Figure S16. χT = f(T) for **1** before (left) and after (right) irradiation

Accepted Manuscript